GRAPHICAL ABSTRACT

Understanding Inconsistencies in Thermohydraulic Characteristics Between Experimental and Numerical Data for DI Water Flow Through a Rectangular Microchannel

Mark Schepperle, Nima Samkhaniani, Mirco Magnini, Peter Woias, Alexander Stroh

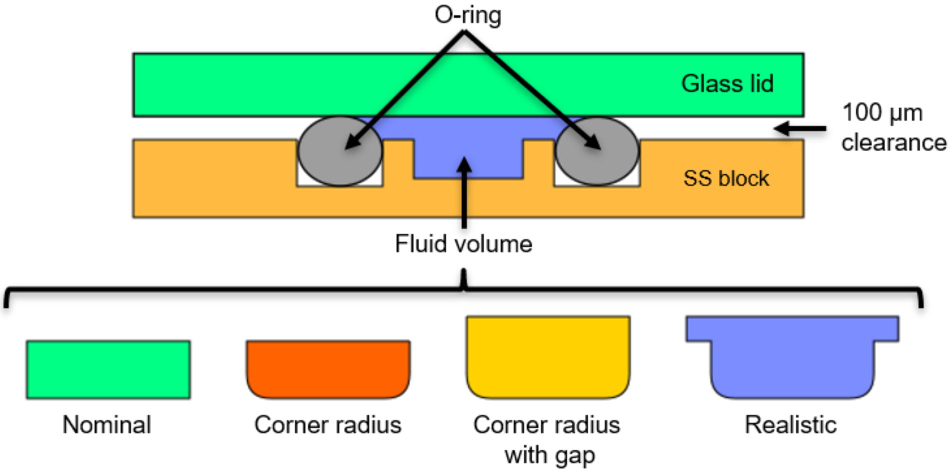

HIGHLIGHTS

Understanding Inconsistencies in Thermohydraulic Characteristics Between Experimental and Numerical Data for DI Water Flow Through a Rectangular Microchannel

Mark Schepperle, Nima Samkhaniani, Mirco Magnini, Peter Woias, Alexander Stroh

- Consideration of geometrical measurement uncertainties and inlet/outlet losses resolves pressure drop inconsistencies.
- Measurement uncertainties are dominated by the geometrical details of microchannel cross section.
- Entrance region length plays a crucial role in the flow development in microchannels and translates into deviation of pressure drop measurement from the theoretical laminar values.
- Heat transfer discrepancies are mainly linked to the estimation uncertainty of air heat transfer coefficient in simulation's outer boundary conditions.

Understanding Inconsistencies in Thermohydraulic Characteristics Between Experimental and Numerical Data for DI Water Flow Through a Rectangular Microchannel

Mark Schepperle[a], Nima Samkhaniani[b], Mirco Magnini[c], Peter Woias[a], Alexander Stroh[b]

[a]*Laboratory for Design of Microsystems, Department of Microsystems Engineering, University of Freiburg, Georges-Koehler-Allee 102, Freiburg, 79110, Germany, Correspondence: schepperle@imtek.de*
[b]*Institute of Fluid Mechanics, Karlsruhe Institute of Technology (KIT), Kaiserstr. 10, Karlsruhe, 76131, Germany*
[c]*Department of Mechanical, Materials and Manufacturing Engineering, University of Nottingham, Nottingham NG72RD, United Kingdom*

ABSTRACT

Facing discrepancies between numerical simulation, experimental measurement and theory is common in studies of fluid flow and heat transfer in microchannels. The cause of these discrepancies is often linked to the transition from the macro-scale to the micro-scale, where the flow dynamics might be expected to deviate due to possible change in dominant forces. In this work, an attempt is made to achieve agreement between experiment, numerical simulation and theoretical description within the usual framework of laminar flow theory. For this purpose, the pressure drop, friction factor, and Poiseuille number under isothermal conditions and the temperature profile, heat transfer coefficient, Nusselt number, and thermal performance index under diabatic conditions (heating power of 10 W*) in a heat sink with a stainless steel microchannel with a hydraulic diameter of 850* μm *were investigated numerically and experimentally for mass flow rates between 1 and 68* $\mathrm{g\,min^{-1}}$*. The source of inconsistencies in pressure drop characteristics is found to be linked to the geometrical details of the utilized microchannel, e.g. the design of inlet/outlet manifolds, the artefacts of manufacturing technique and other features of theexperimental test rig. For the heat transfer characteristics it is identified, that an appropriate estimation of the outer boundary condition for the numerical simulation remains the crucial challenge to obtain a reasonable agreement. The manuscript provides a detailed overview of how to account for these details to mitigate the discrepancies and to establish a handshake between experiments, numerical simulations, and theory.*

Keywords: microchannel, OpenFOAM, single phase, friction factor, heat transfer, development length, measurement uncertainties

1. INTRODUCTION

The behavior of fluid flow in microchannels has been a longstanding topic of interest in the field of fluid dynamics and heat transfer [1]. Specifically, researchers investigated whether the fluid flow in microchannels behaves similarly to a conventional laminar flow or whether there are deviations from this theoretical description and what the reasons for these possible deviations might be. This question is of great importance because of the huge potential of microchannel applications in various engineering systems, such as cooling systems for electronic devices or in chemical process engineering to provide high quality steam. To better understand the behavior of fluid flow and heat transfer in microchannels, researchers have conducted numerous experimental studies [2, 3]. The results of these studies vary, with some showing deviations from the laminar flow theory [4, 5] and others supporting its validity [6, 7].

Some studies have shown that flow and heat transfer in the microscale often deviate from conventional laminar flow theory due to scaling effects such as surface roughness and entrance effects. For example, Peng *et al.* [8] investigated the flow characteristics of water flowing through rectangular microchannels and found that the friction factor (f) deviates significantly from the conventional laminar flow theory. Later, Peng and Peterson [4] studied the effect of channel size on single-phase flow in heated microchannels using water and methanol as working fluids. They claimed that laminar-to-turbulent flow transition occurs at a Reynolds number (Re) of $Re \geq 300$ and a fully developed turbulent flow regime was first obtained at $Re > 1000$. In another study, Pfund *et al.* [9] conducted an experiment to measure pressure drop across a microchannel and identified different flow regimes for water as a working fluid. The onset of laminar-to-turbulent flow transition was found at a Re range of $1500-2200$, and the Poiseuille number ($Po = fRe$) was found to be significantly higher than the theoretical value for fully developed laminar flow, but the authors remained uncertain about which parameter, channel geometry or surface roughness, had a stronger effect on Po due to experimental uncertainty.

Contrary to the observations discussed above, some studies have found no significant deviations from conventional laminar flow theory. For instance, Judy *et al.* [6] found no significant deviations from conventional laminar flow theory when investigating single-phase pressure drop in circular and square microchannels with diameters ranging from 0.015 to 0.15 mm and lengths ranging from 36 to 300 mm. Mokrani *et al.* [10] also conclude that conventional laws and correlations are applicable to low aspect ratio rectangular microchannels with hydraulic diameters less than 0.1 mm. They also report no effect of hydraulic diameter on the Nusselt number in their study. Rosa *et al.* [7] investigate scaling effects on single-phase flow in microchannels and conclude that macroscale theory and correlations are valid at the microscale if measurement uncertainty and scaling effects were carefully considered. These scaling effects include entrance effects, viscous heating, conjugate heat transfer, electric double-layer effects, surface roughness, and temperature-dependent properties [3].

As described in the aforementioned studies, the uncertainty associated with experimental measurements is a crucial factor that needs to be considered in microchannel research, since even small errors in measurements might lead to significant deviations in results, making it difficult to draw meaningful conclusions. This highlights the importance of utilizing numerical simulations as a tool to better understand fluid flow and heat transfer in microchannels [2]. Numerical simulations allow for the configuration of different operational conditions and provide insight into the behavior of fluids at microscales. By incorporating the relevant physics and geometry of the microchannel, numerical simulations can help researchers to interpret their experimental observations and provide a deeper understanding of the underlying mechanisms that govern fluid flow and heat transfer in microchannels. For example, Lee *et al.* [11] found no significant difference between the predictions made by the fully conjugated model and the thin-wall model for microchannels with a rectangular cross-sectional area. On the other hand, Sahar *et al.* [12] found that the uniform heat flux assumption was not valid, and the deviation between the experimental results and the 3D fully conjugated model was attributed to the non-uniform distribution of heat flux along the channel. Dharaiya and Kandlikar [13] report that the effects on Nu in the entry region of the developing flow are insignificant. Additionally, Gunnasegaran *et al.* [14] report that the rectangular channel with the smallest hydraulic diameter had the highest

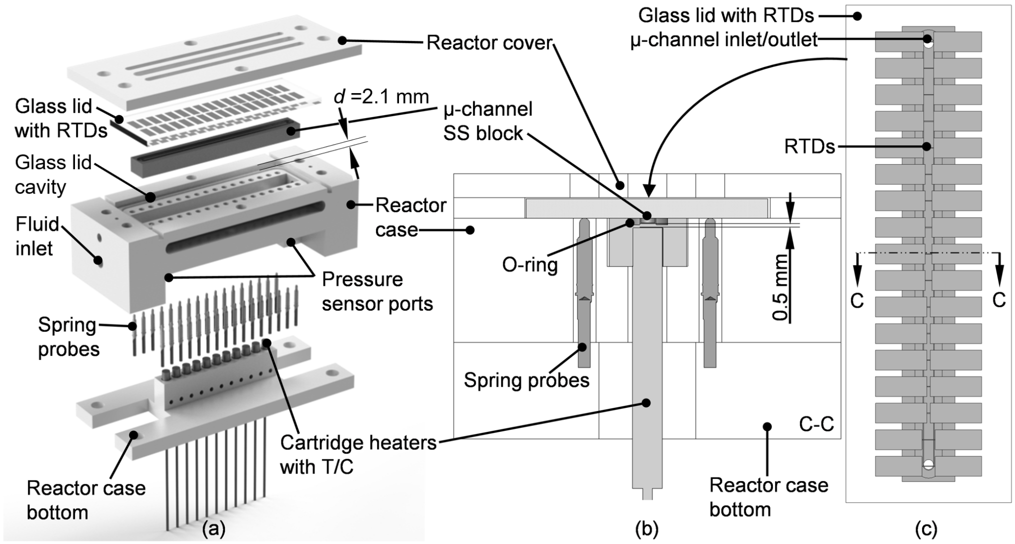

Figure 1: Microchannel setup: exploded view (a), the cross-sectional view (b) and top view on the glass lid with RTDs above the SS microchannel block (c)

heat transfer coefficient, while Sahar *et al.* [15] showed the thermal performance index should be taken into consideration in the analysis of the thermohydraulic performance of microchannels heat exchangers. Pan *et al.* [16] report the existence of the optimal aspect ratio in which the heat transfer performance of the microchannel heat sink reaches its peak. The optimal aspect ratio is found to be different for various working fluids and solid materials. However, it is worth noting that accurately modeling the behavior of fluid flow and heat transfer in microchannels can be challenging. This is mostly linked to the very small length scales and the fact that the flow can be influenced by various factors such as entrance effects, viscous heating, conjugate heat transfer, heat losses, surface roughness, inlet/outlet restrictions and pressure sensors placed outside the microchannel [17, 18]. Additionally, concerting experimental and numerical study with the same conditions inside a microchannel might be difficult due to the uncertainty in the geometry of the channel.

In the present study, we investigate the pressure drop, temperature profile and heat transfer for DI water flow in a rectangular microchannel with a hydraulic diameter of 850 μm in the Reynolds number range up to $Re \approx 1100$ by means of experiments and fully resolved 3D simulations of the microchannel system including inlet and outlet manifolds and conjugate heat transfer. Our main objective is to contribute to the understanding of the behaviour of fluid flow and heat transfer in microchannels through a concerted experimental-numerical study, by identifying the reasons for the observed discrepancies and the ways to resolve them.

2. EXPERIMENTAL METHODOLOGY

In the experimental part of this study, isothermal pressure drop at 22.7 °C and temperature profile at a heating power of 10 W in a 492 μm high, 1.5 mm wide and 65 mm long rectangular stainless steel (SS) microchannel with a hydraulic diameter of 848.9 μm is measured. The mass flow rate ranges from 1 to 68 $\mathrm{g\,min^{-1}}$ for pressure drop measurements in isothermal cases and from 1 to 49 $\mathrm{g\,min^{-1}}$ for temperature profile measurements in diabatic cases. This corresponds to Reynolds numbers between 16 and 1144. Deionized (DI) water is used as the working fluid.

2.1. Experimental Apparatus

Fig. 1 shows the considered microchannel heat sink with integrated resistance temperature detectors (RTDs) to measure the temperature profile along the microchannel and cartridge heaters [19] to heat up the microchannel. The same experimental apparatus has been used in a set of studies reported in [20, 21, 22, 23]. The heat sink housing is specifically designed for mechanical fixation of the microchannel, RTDs and cartridge heaters, for hermetic sealing of the microchannel and for thermal insulation from the environment. A fluid reservoir storing DI water at room temperature is connected to a micro annular gear pump mzr-4622 from HNP Mikrosysteme GmbH [24]. This pump supplies the DI water with low pulsation and at well-defined flow rates to the heat sink with the SS microchannel. The low pulsation of the micropump intends to reduce pressure oscillations during pressure drop measurements. A 10 µm particle filter is placed in front of the micropump to prevent contaminants from entering the microchannel heat sink. The heat sink outlet is connected to a wastewater reservoir with a high-precision balance to accurately determine the mass flow rate. The wastewater reservoir is primarily important during temperature profile measurements, since in closed-loop configurations, where the heated fluid at the outlet of the heat sink flows back into the fluid reservoir, the fluid temperature at the heat sink inlet would increase over time.

The rectangular microchannel (492 ± 5 µm × 1.5 mm × 65 mm) was fabricated in a 1.4404 / 316L SS block (5 mm × 8 mm × 68.6 mm) by machining and mounted in the heat sink housing as shown in Fig. 1a and Fig. 1b. The DI water is supplied and discharged via two holes at the ends of the machined microchannel, each leading to an inlet and outlet on the heat sink housing. The heating power required for the temperature profile and heat transfer analysis is applied via eleven resistive cartridge heaters located directly below the microchannel. The cartridge heaters are mounted in 4 mm deep holes along the bottom of the microchannel plate and fixed in the bottom plate of the heat sink housing with thermally insulating PEEK screws. They carry integrated type K thermocouples (T/C) in their top tips measuring the temperatures at the points of contact between the T/C and the microchannel block. The RTDs shown in Fig. 1c are fabricated in a clean room process on a Pyrex glass lid (2 mm × 25 mm × 75 mm) [20], which is pressed onto the microchannel plate from above by means of the heat sink housing lid. An O-ring in a groove surrounding the microchannel provides a hermetic seal between the microchannel and the glass lid. The heat sink housing surrounding the microchannel is fabricated by laser stereolithography from a high-temperature stable, inert resin with a low thermal conductivity of 0.62 $\mathrm{W\,m^{-1}\,K^{-1}}$ (at 23 °C) [25]. On both sides of the resin housing, parallel to the longitudinal axis of the microchannel, there are 17 holes each, in which a total of 32 low-resistance spring contacts are anchored [26]. These spring contacts established electrical contact with up to 17 RTDs when the glass lid is pressed on. This allows a high spatial resolution of the inside glass lid temperature along the microchannel, which could be compared with the temperature measurements of the T/C at the tips of the cartridge heaters and the numerical simulation data (see Section 3). The temperature at the outer surface of the heat sink was measured using the benchtop thermal camera FLIR A65SC from Teledyne FLIR with a spatial resolution of 1.31 mrad and an accuracy ±5 % of reading.

Fig. 2 shows the details of utilized microchannel. Due to the corner radius of 0.2 mm of the milling tool used for channel milling, the geometry of microchannel is not exactly rectangular.

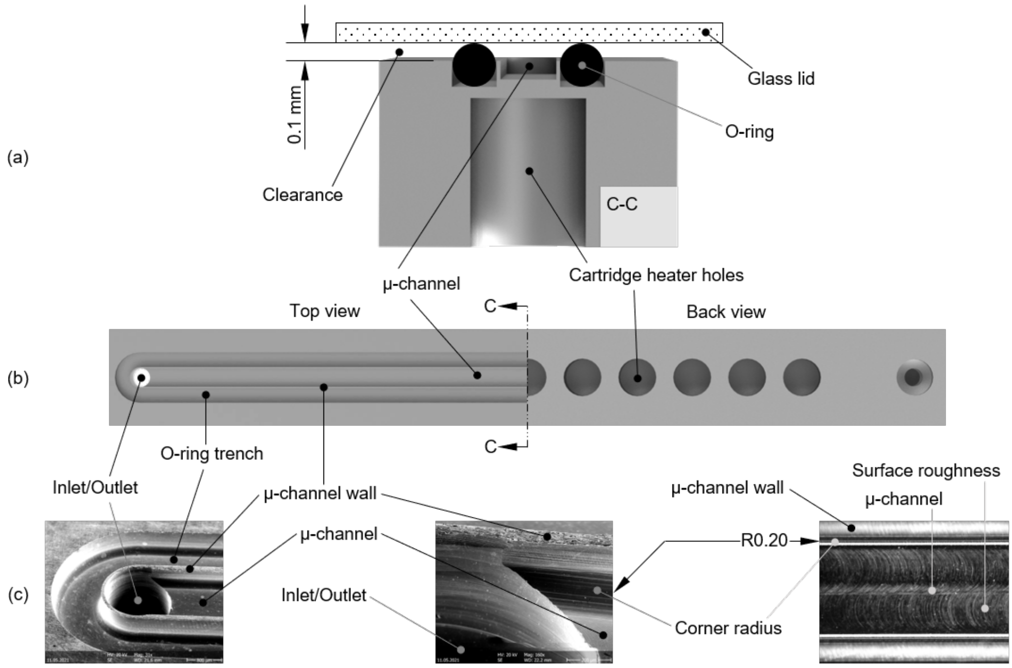

Figure 2: Stainless-steel microchannel: Cross-sectional view (a), top and bottom view (b) and scanning electron microscope images of the inlet with channel wall and surrounding O-ring cavity (left), the corner radius at the inlet (center) and the surface roughness of the channel bottom (right) (c)

This is clearly visible in Fig. 2c in the rounded corners between the channel wall and the channel bottom surface. Based on the measurements using atomic force microscopy, the surface roughness of the channel bottom is 55 ± 23 nm. The fit between the glass lid and the heat sink cavity for the glass lid is estimated to be 100 ± 50 µm: the depth d of the rectangular cavity for the glass lid in the 3D printed reactor case is 2.1 mm (see Fig. 1) with an uncertainty of ± 50 µm caused by the 3D printing process with the glass lid being 2.0 mm thick. As shown in Fig. 2a, this clearance ensured that the RTDs do not directly rest on the top of the channel block. This is because direct contact between glass lid and the SS channel block could cause an electrical short circuit of the RTDs and mechanically damage these structures as well as the glass lid, leading to a distortion of the measured resistance and leakage. It has to be noted that the introduced clearance height is unknown and may vary among different experimental campaigns. We estimate that this additional clearance increases the height of the microchannel from 492 ± 5 µm to 592 ± 50 µm. More information on the properties of RTDs can be found in [20].

2.2. Metrological Characterization

The isothermal pressure drop from the inlet to the outlet of the microchannel is determined using a differential pressure transducer with compensated line pressure and temperature dependency [27]. The compensation for line pressure is important as the line pressure changes over time with the level of the DI water and wastewater reservoir altering the pressure drop measurement. The differential pressure transducer is connected to fluidic ports located at the bottom of the heat sink housing as shown in Fig. 1a and 5. The heat sink inlet and outlet meet through-holes

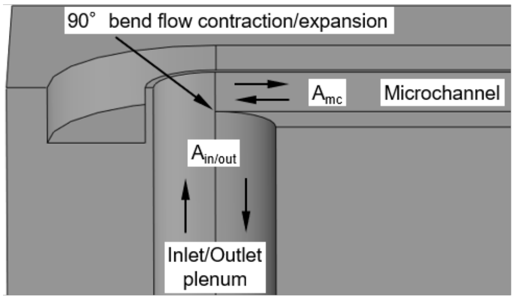

Figure 3: 90° bend causing pressure loss at the microchannel inlet plenum due to flow contraction and pressure recovery at the microchannel outlet plenum due to flow expansion

inside the heat sink which acted as fluidic tees and lead the DI water to the pressure transducer ports and the microchannel inlet/outlet. The indicated mass flows are determined with the precision balance at the wastewater reservoir. For this purpose, the micro annular gear pump was run for 60 s and the weight difference was determined. The mass flow rate corresponds to the weight difference divided by the time. The effect of evaporation from the free liquid surface of DI water in the wastewater reservoir was investigated by measuring the change in weight during the test period of 60 s with the pump turned off. There was no change in the measured weight, so the influence of evaporation on the measured weight difference during the test period is confirmed to be negligible. This is also consistent with the result reported in a similar study [6].

To obtain the pressure loss along the entire microchannel Δp_{mc} from the differential pressure measurements, the pressure losses at the inlet Δp_{in} and outlet of the microchannel Δp_{out} have to be subtracted from the measured differential pressure Δp_{tot} (see Fig. 5a):

$$\Delta p_{mc} = \Delta p_{tot} - \Delta p_{in} - \Delta p_{out}. \tag{1}$$

The pressure losses are computed based on the model by Lee and Garimella (2008) [28]. The detailed description for estimation of pressure losses and material properties can be found in APPENDIX A.

The temperature profile along the microchannel was determined in steady-state conditions at a total heating power of 10 W in three different ways. Steady-state conditions are assumed after the measured temperature profile remained unchanged for a certain prescribed flow rate. For most flow rates, this occurred no later than two hours after the start of the experimental measurement. The first temperature measurement method utilized the T/C at the tip of the cartridge heaters which are recessed at the bottom of the channel. The second temperature measurement is conducted with the RTDs along the glass lid on the top wall of the microchannel and the third measurement method uses a thermal imaging camera FLIR A65sc above the glass lid. In addition, the fluid temperature is measured directly at the heat sink outlet (approx. 18 mm downstream of the microchannel outlet) with a type T thermocouple.

The total heating power of 10 W is supplied by the cartridge heaters at the bottom of the microchannel for all measurements with cartridge heaters connected in series. Due to the production-related slight variations in the internal resistance of the cartridges (standard deviation of ± 4.4 %), the exact heat output of each cartridge is calculated by its weighted internal resistance relatively to the applied 10 W. The cartridges are positioned according to increasing heating output (860 - 984 mW) from the inlet to the outlet of the system. This helps to reduce the fluctuations in the

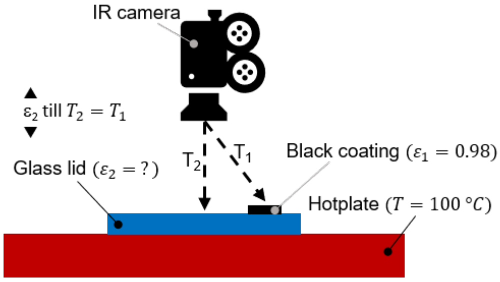

Figure 4: Schematic of Pyrex glass emissivity measurement procedure using a thermal imaging camera (IR camera). The emissivity ϵ_2 of the glass lid is determined by measuring the temperature T_1 of the glass lid with a black coating with a known emissivity ϵ_1 and by matching the temperature measurement of the glass lid without black coating immediately adjacent to the coating T_2 by adjusting the emissivity of the camera till $T_2 = T_1$

.

temperature profile along the channel linked to variations of cartridge heating powers. The exact heat output of the cartridge heaters are used during the numerical simulation as data reduction method to reconstruct the average microchannel wall temperatures given in Fig. 18. The first and last heating cartridges were positioned 9.25 mm from the microchannel inlet and outlet, respectively. Each heating cartridge has a diameter of 3.1 mm and a distance of 4.5 mm from its center to the center of an adjacent cartridge.

The first and the last RTD on the glass cover are located directly above the inlet and outlet of the microchannel, respectively. Each RTD has a width of 0.1 mm and a center-to-center separation of 4 mm. The RTD temperatures are calculated with the following equation using the measured resistances R of the RTDs:

$$T = T_{RT} + \frac{\Delta R}{R_{RT} \cdot \alpha}, \tag{2}$$

where T_{RT} is the room temperature, R_{RT} is the resistance at room temperature, $\Delta R = R - R_{RT}$ with the measured resistance R and $\alpha = 2.98 \cdot 10^{-3}$ °C^{-1} [20].

The thermal imaging camera has been calibrated through following procedure. Firstly, the temperature of 26 °C reflected from the laboratory environment has been measured using a planar crumpled aluminum foil placed directly over the glass cover. Next, the emissivity ϵ_2 of the glass lid has been determined as shown in Fig. 4 through local application of a black coating spray with an emissivity ϵ_1 of 0.98 on a glass lid. First, the emissivity of the thermal imaging camera was set to 0.98 the emissivity of the black coating. Then, the glass lid was heated to approximately 100 °C on a hotplate and the temperature T_1 of the black coating was measured with the thermal imaging camera, so a subsequent adjustment of the camera's emissivity until the full temperature correspondence $T_2 = T_1$ can be performed with T_2 being the temperature of a glass lid spot without black coating immediately adjacent to the coating. In this process the glass lid emissivity ϵ_2 was determined to be 0.89. This value depends on the exact composition of the borosilicate glass and is comparable to emissivities found in the literature, e.g. 0.82 for Pyrex [29].

A detailed consideration of all experimental uncertainties is of great importance in order to make a correct statement about the agreement of experimental measurement results with the numerical simulations. The summary of uncertainties for the measured quantities is listed in Tab. 1. Uncertainties of quantities that are derived from other measured quantities are calculated

Table 1: Uncertainties of experimental measurement

quantity	uncertainty	measurement device
mass flow rate (M)	u_M = ± 2 µg s^{-1}	high-precision balance
differential pressure (Δp_{tot})	$u_{\Delta p_{tot}}$ = ± 35 Pa (0-35 kPa)	theoretical
microchannel width (W_{mc})	$u_{W_{mc}}$ = ± 1 µm	theoretical
microchannel height (H_{mc})	$u_{H_{mc}}$ = ± 5 µm	optical microscope
microchannel inlet diameter (d_{in})	$u_{d_{in}}$ = ± 10 µm	optical microscope
microchannel outlet diameter (d_{out})	$u_{d_{out}}$ = ± 10 µm	optical microscope
microchannel to heat sink lid fit (H_{fit})	$u_{H_{fit}}$ = ± 50 µm	theoretical
T/C type K temperature (T_K)	u_{T_K} = ± 1.5 °C	theoretical
T/C type T temperature (T_T)	u_{T_T} = ± 0.5 °C	theoretical
RTD temperature (T_R)	u_{T_R} = ± 0.5 °C	calculated [20]
water reservoir temperature (T_{H_2O})	$u_{T_{H_2O}}$ = ± 1.1 °C	T/C type T

according to the German industrial standard DIN 1319-3 [30] using the following equation for the uncertainty propagation:

$$u_y = \sqrt{\sum_{i=1}^{n} \left(\frac{\partial y}{\partial \sigma_i} u_{\sigma_i} \right)^2}, \tag{3}$$

where u_y is the estimated uncertainty for y, σ_i represents the measurement values used to calculate y and u_{σ_i} stands for the uncertainties of measurement values. Since the mathematical formulations for the measurement uncertainties derived from Equation 3 are quite extensive, they are listed in APPENDIX B, which is intended to serve to the reader as a reference for identical or similar experimental trials.

3. NUMERICAL METHODOLOGY

In this section, we provide a description of the models employed as a numerical counterpart for the investigation of the heat transfer and fluid dynamics within the microchannel heat sink.

3.1. Geometrical Description and Mesh Generation

To simplify the computational process and reduce computational costs, the geometry considered in the numerical simulation consists solely of the core of the heat sink, excluding other components present in the experimental setup described earlier. For isothermal simulations, the model considers only the liquid region in the heat sink i.e. microchannel, including cylindrical inlet and outlet manifolds and a semi-rectangular microchannel as shown in Fig. 5a. The fluid enters and leaves the channel vertically (y-axis), in a direction normal to the channel axis (x-axis). The inlet/outlet manifolds and channel dimensions correspond to the ones described in the experiment section. For diabatic simulation, the model considers the whole metal SS block region with heaters placed in the cylindrical blind holes at the bottom of the metal block as shown in Fig. 5b. Here, the fluid region includes the microchannel and inlet/outlet plenums without pressure ports. The glass lid is modeled through the application of a special boundary condition placed at the top wall of the microchannel as described in the following section.

It has to be noted that the true shape of the cross-sectional area within the microchannel is unknown. As depicted in Fig. 6, we expect a deviation from the nominal shape to be present.

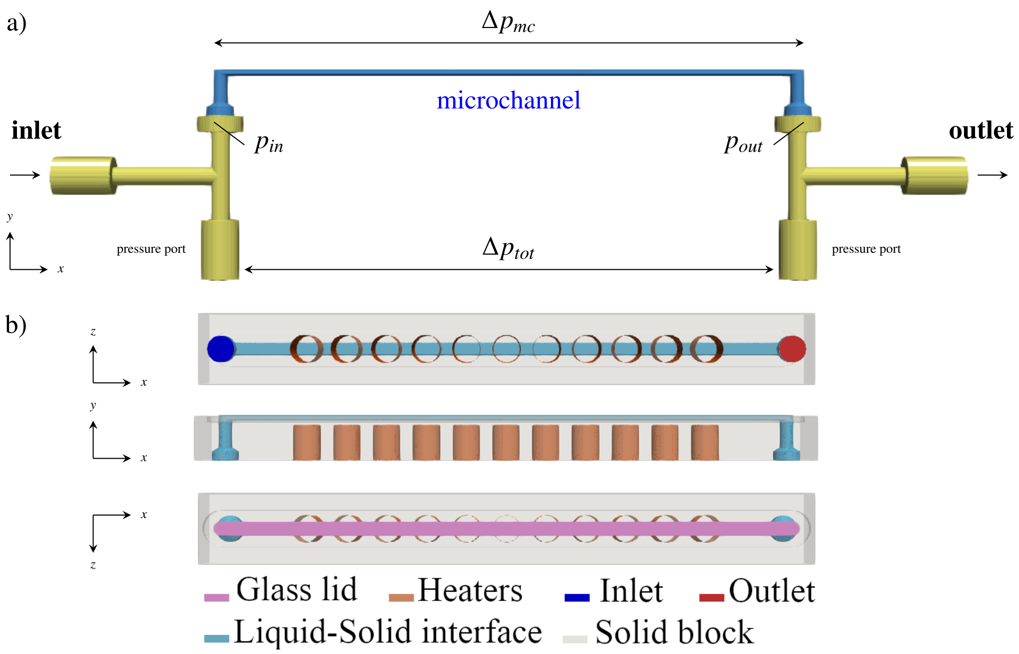

Figure 5: Numerical domain schematics: a) isothermal simulation for simpleFoam b) diabatic simulation for chtMultiRegionFoam

While the nominal cross-section of the microchannel is typically assumed to be rectangular, in reality, the bottom of the microchannel has curved corners as a result of the milling process, and the height of the channel is slightly greater due to the clearance gap between the glass lid and the heat sink block. Therefore, different levels of abstraction for the cross-sectional geometries were examined to select the optimal combination for the numerical setup by comparing the numerical result with the experiment (see Section 4.1.1). The final configuration incorporates both the curved corners and the additional gap size H_{fit} (corresponding to the cross-section shaded in yellow color in Fig. 6) to better represent the real-world conditions and improve the accuracy of our numerical simulations. By incorporating these considerations, we aim to accurately capture the heat transfer and fluid dynamics phenomena within the microchannel heat sink while managing computational complexity and ensuring computational efficiency.

Both isothermal and diabatic simulations were carried out using the open-source computational fluid dynamics (CFD) package OpenFOAM-7 [31]. The geometric models for the simulations were generated using OpenFOAM's mesh generators, namely blockMesh and snappyHexMesh. The number of cells for isothermal and diabatic simulations is around 1.6 million and 2.2 million cells, respectively, resulting in a 12×24 cell configuration for $H \times W_{mc}$ for the microchannel. To ensure the accuracy of the simulation results, a grid independence study is conducted. This configuration guarantees that the dimensionless wall distance y^+ for the first cell of the microchannel never exceeds the value of 2.5. Figure 7 depicts the grid used in the diabatic simulations for the solid and the fluid region.

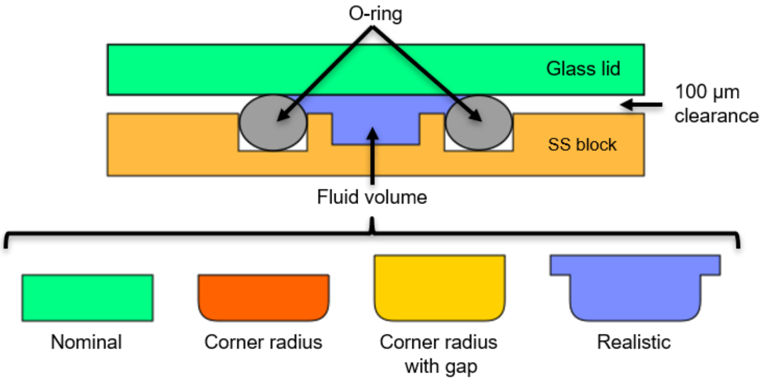

Figure 6: Numerical abstraction of the cross-sectional area (respectively fluid volume) of the experimental microchannel with increasing consideration of geometric details from left (nominal) to right (realistic). The third cross-sectional shape colored in yellow is utilized in the final numerical simulation.

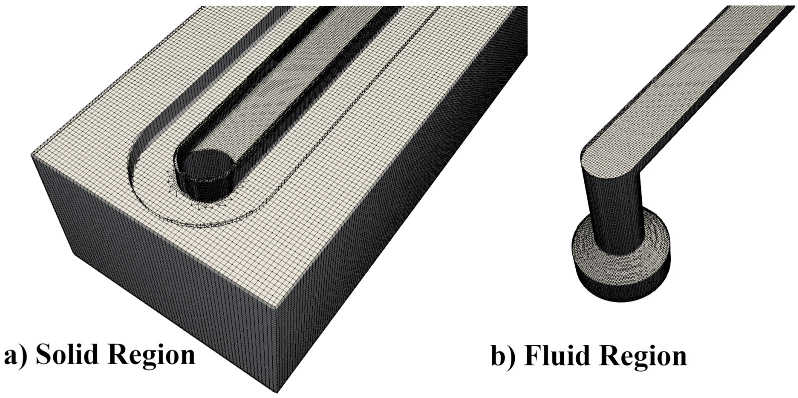

Figure 7: A sample of the grid for conjugate heat transfer simulation using chtMultiRegionFoam

Table 2: Physical properties of water utilized in simulation

θ	$a_{\theta,0}$	$a_{\theta,1}$	$a_{\theta,2}$	$a_{\theta,3}$
ρ	746.025	1.93	−0.003654	0
μ	0.116947	−0.001	$2.9 \cdot 10^{-6}$	$-2.8 \cdot 10^{-9}$
c_p	9850.69	−48.67	0.1374	−0.000127
κ	−0.7107	0.007186	$-9.298 \cdot 10^{-6}$	0

3.2. Boundary Conditions and Solution Procedure

In isothermal simulations, the governing equations are solved only in the fluid region. The fluid is incompressible and laminar, and the simulations are conducted with the solver simpleFoam from the OpenFOAM-7 framework [31]. The physical properties of the working fluid are considered constant at room temperature, since only hydraulic effects are of interest in the isothermal case. In diabatic simulations, the simulation is performed with the solver chtMultiRegionFoam. In this case, in addition to the continuity and momentum equations which are solved for the fluid region, the energy equation is solved for both solid and fluid regions. In the numerical simulation, the convection terms in the governing equations are discretized using first-order upwind schemes. This choice is made to prioritize faster convergence of the solution. It has been found that using second-order schemes APPENDIX C does not significantly improve the accuracy of the results. Therefore, the use of first-order upwind schemes is considered sufficient for the purposes of the simulation. The steady-state simulations are performed using convergence criteria of 10^{-6}, which was confirmed to provide the same solution compared to the simulations with lower convergence criteria. The physical properties, including density, specific heat, dynamic viscosity, and thermal conductivity, are computed using polynomials that fit the water properties in the temperature range between 0 °C to 100 °C, as given by:

$$\theta(T) = \theta_{\theta,0} + a_{\theta,1} \cdot T + a_{\theta,2} \cdot T^2 + a_{\theta,3} \cdot T^3, \theta \in \{\rho, c_p, \mu, \kappa\}, \tag{4}$$

where the coefficients $a_{\theta,i}$ are summarized for the quantity θ in the Tab. 2.

The flowRateInletVelocity boundary condition is applied to impose a constant velocity value ($|\vec{v}| = M/\rho A_{mc}$) at inlet that matches the specified mass flow rate M according to the experiment. At the walls, a noSlip condition ($\vec{v} = (0, 0, 0)$) is employed. The outlet uses the pressureInletOutletVelocity condition, which applies a zero-gradient condition for outflow ($\partial\vec{v}/\partial n = 0$) or assigns a velocity based on the flux in the patch-normal direction in the case of inflow, the pressure is specified with totalPressure ($p = p_0 - |\vec{v}|^2/2$) with $p_0 = 0$. For the inlet and walls, a zero-gradient condition is applied for the pressure ($\partial p/\partial n = 0$). Here, n represents the normal direction to the patch.

In the diabatic scenario, the temperature at the inlet is constant and corresponds to the room temperature ($T = 22.7$°C). A uniform heat flux is applied to the cylindrical walls of the solid block where the cartridge heaters are directly in contact. The area surrounding the individual heaters is actively heated and the total heating power is $Q = 10$ W. However, it should be noted, as explained in the experimental section, that the heat output of each heat source differs due to the variation in the internal resistance of the respective cartridge, and thus the assumption of a uniform heating source is further examined in a later section. The tips of the cylindrical holes remain unheated in our setup due to the presence of a gap between the cartridges and the solid block. This gap is filled with stagnant air, which has low thermal conductivity ($0.2587 \mathrm{W\,m^{-1}\,K^{-1}}$) consequently, the heat loss from this section is deemed negligible, accounting for less than 1% of the total heat generated, and can be effectively treated as insulated. The boundary condition, turbulentTemperatureCoupledBaffleMixed, is employed for the common wall interface between the liquid-solid regions. Notably, the simulation does not utilize any turbulence model and this boundary condition only ensures the continuity of heat flux ($q_s'' = q_l''$) and temperature profile ($T_s = T_l$) at the common interface. It employs:

$$T_f = \frac{T_{p,s}\left(\frac{\kappa_s}{\delta_s}\right) + T_{p,l}\left(\frac{\kappa_l}{\delta_l}\right)}{\left(\frac{\kappa_s}{\delta_s}\right) + \left(\frac{\kappa_l}{\delta_l}\right)} \tag{5}$$

The external walls of the solid block are subjected to a heat flux condition with a fixed heat transfer coefficient (h). This condition is governed by the externalWallHeatFluxTemperature boundary condition, expressed as:

$$-\kappa\frac{T_p - T_f}{|\delta|} = \frac{T_{am} - T_f}{R_{th}}, \tag{6}$$

Here, T_f represents the temperature at the boundary, T_p is the temperature at the first cell center near the boundary, and δ is the distance between them. The thermal resistance, R_{th}, is calculated as:

$$R_{th} = \frac{1}{h} + \sum_{i=1}^{n} \frac{l_i}{\kappa_i}, \tag{7}$$

The thickness, l_i, and thermal conductivity, κ_i, of surrounding materials are taken into account. The housing has a thermal conductivity of the 0.621 $\mathrm{W\,m^{-1}\,K^{-1}}$ (at 23 °C) [25] and a thickness of 15.6 mm except at the top which is 3.5 mm. The same boundary condition is applied at the microchannel top to account for the presence of the glass lid which has a thickness of 2 mm and a thermal conductivity of 1.2 $\mathrm{W\,m^{-1}\,K^{-1}}$. An assumed ambient air heat transfer coefficient of 25 $\mathrm{W\,m^{-2}\,K^{-1}}$ is used. The impact of this assumption is examined in Section 4.2.2.

4. RESULT AND DISCUSSION

4.1. Isothermal Study

In this section, the numerical and experimental results related to the effects of mass flow variation on the pressure drop under isothermal conditions and on the temperature profile and local heat transfer along the microchannel under diabatic conditions are compared and discussed. The focus of the discussion is on identifying and resolving possible causes of inadequacies in experimental measurements and numerical simulations.

4.1.1. Influence of Microchannel Cross-section

Fig. 8 shows the pressure drop from numerical simulations evaluated for the different cross-section abstraction levels (Fig. 6) of the experimental microchannel. By comparing the microchannel pressure drop curve for the nominal cross-section with the pressure drop curve where the corner radius of 0.2 mm at the microchannel bottom is considered, it can be seen that the corner radius slightly increases the numerically simulated microchannel pressure drop. If the microchannel clearance of 100 µm between the microchannel and the glass lid is added (corner radius with gap) the simulated pressure drop reduces significantly. However, considering

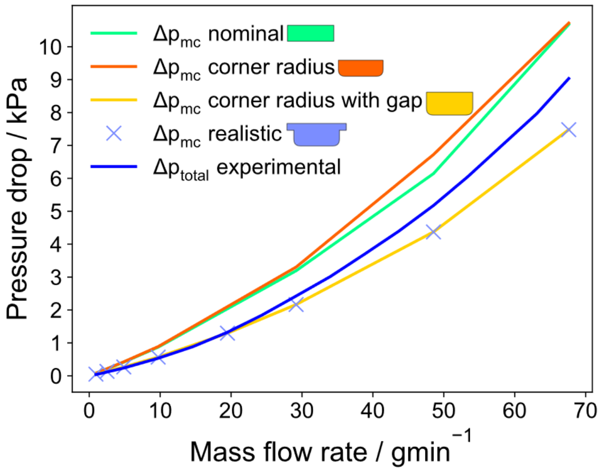

Figure 8: Numerically simulated microchannel pressure drop for the microchannel abstraction levels shown in Fig. 6 together with the experimentally measured pressure drop Δp_{tot}

the small fluid volume above the microchannel walls caused by the 100 µm clearance between the microchannel and the glass lid (blue curve) has no significant effect on the microchannel pressure drop and can be neglected. The consideration of geometric details of the microchannel such as the corner radius and the gap are thus essential to obtain a match between numerically simulated and experimentally measured pressure drop. However, the experimentally measured pressure drop Δp_{tot} still deviates from the numerical pressure drop of the corner radius with the gap domain and the realistic domain with increasing mass flow rate, although geometric details are considered in the simulation. By subtracting the pressure losses at the 90 ° bends of the microchannel inlet and outlet (Fig. 3) from the experimentally measured pressure drop Δp_{tot} using Eq. 1, this deviation can be eliminated. This is discussed in detail in the next section.

4.1.2. Pressure Loss Contributions

In Fig. 9a the experimentally measured pressure drop Δp_{tot} and the pressure drop Δp_{mc} experienced in the microchannel and calculated according to Eq. 1 are compared with the pressure drop extracted from the corresponding numerical simulations. All numerical simulations are plotted for the corner radius with gap domain shown in Fig. 6 in yellow.

When comparing the profile of the measured pressure drop Δp_{tot} with the simulated pressure drop Δp_{mc}, an increasing deviation can be observed with increasing flow rate. This can be attributed to the growing pressure losses at the 90°-bends of the inlet and outlet manifolds, which are also included in the measurement due to the position of the pressure transducer connection ports on the bottom side of the heat sink (Fig. 1). A look at Fig. 9a shows, however, that these can be reliably estimated using the data reduction method by Lee and Garimella [28] to calculate Δp_{in} and Δp_{out} (see APPENDIX A). It is important to note that such pressure losses lead to significant discrepancies between numerical and experimental results and should therefore be carefully considered. The influence of the fluidic tees at the inlet and outlet of the heat sink, which divide the DI water flow to the microchannel and to the pressure ports, the fluidic path to the pressure ports (Fig. 5) and the piping from the pressure ports to the pressure transducer were

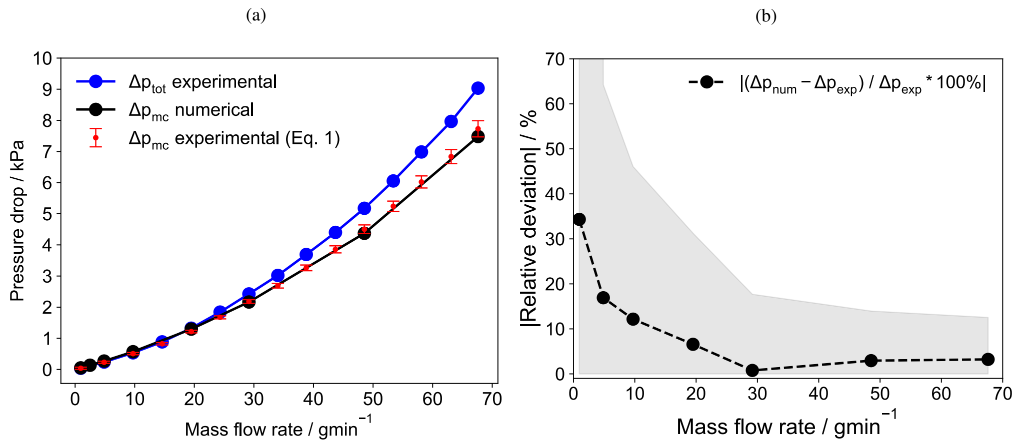

Figure 9: (a) Experimental and numerical pressure drop; (b) Magnitude of the relative deviation = $100\% \cdot |(\Delta p_{num} - \Delta p_{exp}) / \Delta p_{exp}|$ of the pressure drop simulation from the pressure drop calculated with Eq. 1. The gray shaded area marks the uncertainty area $100\% \cdot |(\Delta p_{num} - \Delta p_{exp} \pm u_{\Delta p_{mc}})/(\Delta p_{exp} \pm u_{\Delta p_{mc}})|$ linked to the experimental measurement uncertainty $u_{\Delta p_{mc}}$ calculated with Eq. 36 as given in APPENDIX B.

negligible in both experiment and simulation and did not lead to any significant deviation.

The magnitude of the relative deviation of the numerical simulation from the experimental pressure drop Δp_{mc} is shown in Fig. 9b. At the lowest flow rate of 1 g min^{-1}, where the measured differential pressure is only 38 Pa, the measurement approaches the uncertainty of ± 35 Pa of the pressure transducer used (Tab. 1). This results in an uncertainty of the relative deviation magnitude that is at least 92 % (if only the uncertainty of the pressure transducer is considered). However, the relative influence of this measurement uncertainty decreases rapidly with increasing mass flow rate. For example, at 68 g min^{-1} it constitutes only 0.01 %. At the same time, we observe an increase of the absolute measurement uncertainty for Δp_{mc}, since the largest influencing factors are now the cross-sectional microchannel area A_{mc}, the microchannel height H_{mc}, the microchannel width W_{mc} and it scales with the squared mass flux G (see Eqs. 34-36). Nevertheless, at higher flow rates, we observe an overall reduction in the deviation between simulation results and the experimental data. This can be attributed to the fact that the relative uncertainty in the experimental data becomes smaller compared to the absolute value of pressure. As a result, the experimental data gets more reliable and less prone to errors. However, it is important to note that even at high flow rates, the uncertainty related to the microchannel cross-area shape, especially due to the uncertainty of the microchannel clearance $u_{H_{fit}}$ (Tab. 1), might cause discrepancies between the simulation and experimental results. Compared to that, the influence of all other uncertainties in Eqs. 34-36, e.g the uncertainty of the water density u_ρ and the uncertainty of the mass flow rate u_M are negligibly small. The equations for all measurement uncertainties are given in APPENDIX B.

Fig. 10a illustrates the contribution of the inlet and outlet pressure loss (p_{in} + p_{out}, blue bars) estimated from the correlations and the microchannel pressure drop (p_{mc}, red bars) to the total measured pressure Δp_{tot} with increasing mass flow rate. As described above, any change in the flow cross-section, such as contraction at the microchannel inlet or expansion at the microchannel outlet, creates a local pressure loss that is also measured in the experiment and has to be taken

Table 3: Entrance length correlations for different channels

correlation	c_1	c_2	c_3	AR	entrance condition
Atkinson *et al.* [32]					uniform flat profile
tube	0.590	0	0.056	1	
parallel plate	0.625	0	0.044	Inf,0	
Galvis *et al.* [33]					uniform flat profile
microchannel	0.74	0.090	0.0889	1	
	1.00	0.098	0.09890*	2.5	
	1.471	0.034	0.0818	5	
Ahmad and Hassan [34]					connected to
microchannel	0.6	0.14	0.0752	1	large tank
Present study					connected to
microchannel	1.12	0	0.114	0.39	vertical plenum

* there is a typo in the original reference [33]

into account when compared to the simulation data. In the heat sink system at all considered flow rates, the main pressure drop (minimum 85% of Δp_{tot}) occurs in the microchannel.

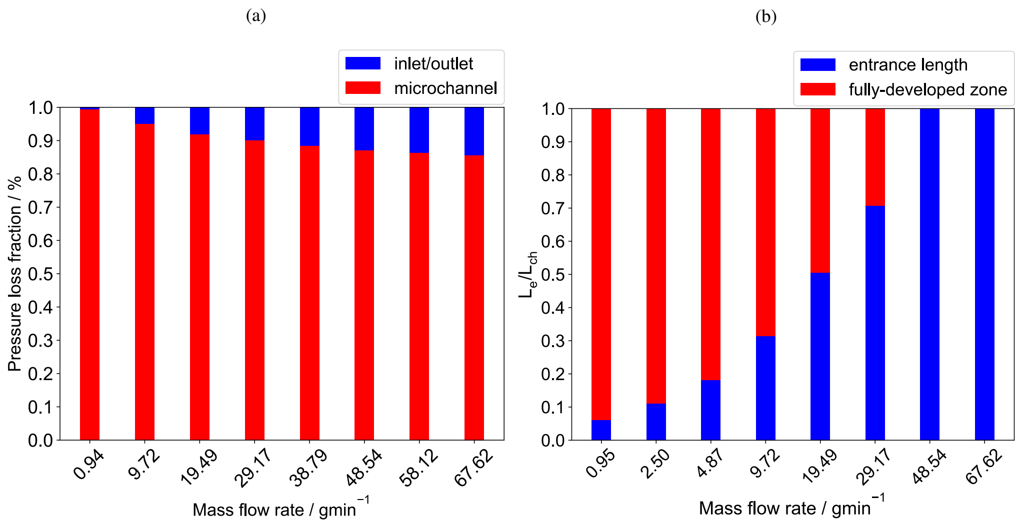

Figure 10: (a) Contribution of the inlet and outlet pressure loss ($p_{in} + p_{out}$, blue area) and the microchannel pressure drop (p_{mc}, red area) to the total experimentally measured pressure Δp_{tot}; (b) Ratio of entrance length to the microchannel length based on numerical simulation

4.1.3. Entrance Length

The flow in the microchannel can be divided into a flow-developing zone, where the velocity profile keeps evolving, and a fully-developed zone where the velocity profile becomes invariant to the streamwise location. The flow-developing zone is often referred to as the hydrodynamic entrance zone and is characterized by its length. The channel entrance zone contributes to the additional pressure loss as the growth in the boundary layer accelerates the flow inside the inviscid central region. Unlike macroscale channels, in microscale devices, the entrance losses can become significant since the developing zone might even occupy the entire length of the channel.

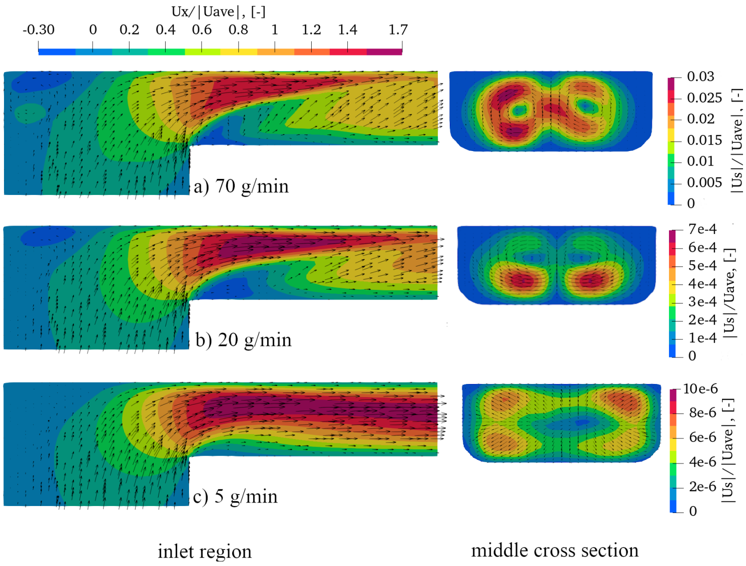

Figure 11: Velocity contour in the 90°-bend: (left) the middle plane at the inlet region, (right) the cross-section in the middle of microchannel at $x = 32.5$ mm

The hydrodynamic entrance length has traditionally been defined as the distance from the channel inlet to the location where the velocity profile reaches 99 % of the fully developed velocity profile [33]. In the present study, this was approximated as the location where the centerline velocity U_c of a developing flow reaches 99 % of the centerline velocity expected in the fully developed profile U_{fd}. In our present study, Fig. 10b shows the fraction of entrance region length relative to the overall length of the microchannel. It covers the entire microchannel length for the two highest mass flow rates considered. The length of the fully-developed zone is a little shorter than what you see in the picture. This is because we didn't exclude the part where the flow is about to leave the channel.

The flow entrance length is primarily influenced by three parameters, namely, the mass flow rate (Reynolds number), the channel aspect ratio (AR), and the inlet velocity profile. Atkinson *et al.* [32] and Chen [35] initially investigated the entrance length in macroscale flows between parallel plates. Recently, some experimental [34, 36] and numerical studies [33, 37] have been conducted to estimate the entrance length in microchannels. A generalized correlation equation for a specified hydraulic diameter is given in [33] as:

$$\frac{L_e}{D_h} = \frac{c_1}{c_2 Re + 1} + c_3 Re, \tag{8}$$

where L_e/D_h represents the dimensionless entrance length and the Reynolds number $Re = MD_h/\mu A_{mc}$ is computed based on the hydraulic diameter which is defined with

$$D_h = \frac{2HW_{mc}}{H + W_{mc}}. \tag{9}$$

In the present study, the hydraulic diameter is $D_h = 846$ µm. It has to be noted that the influence of channel aspect ratio on the dimensionless entrance length is negligible for Reynolds numbers

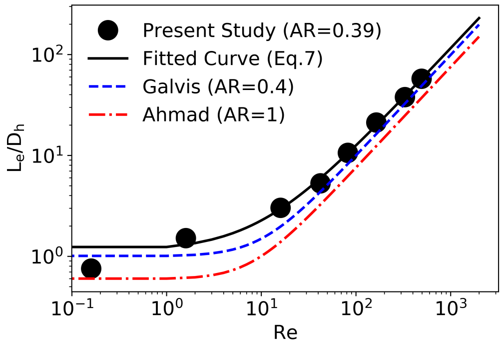

Figure 12: Entrance length of the present numerical study compared with the numerical simulation by Galvis *et al.* [33] and experiments by Ahmad and Hassan [34]. The entrance condition is given in Tab. 3.

$Re > 50$ [33]. The coefficients c_1, c_2, and c_3 are provided in Tab. 3 for various aspect ratios based on the findings of Galvis *et al.* [33]. In numerical studies, the inlet velocity profile is often assumed to be flat, and the choice of inlet conditions significantly affects the entrance length [38]. In practical devices, micro/mini channels are typically preceded by a fluidic element such as a tank or a plenum. Lobo and Chatterjee [37] recently investigated the entrance length of a microchannel connected to a plenum with varying aspect ratios. The authors presented a correlation that accounts for the effect of aspect ratio on the entrance length; however, their correlation is not applicable for low Reynolds numbers (especially for $Re < 20$).

The hydrodynamic development of flows has often been related to the growth of the boundary layer along the channel's walls. However, in the present study, the flow is streaming in/out of the microchannel with a vertical pipe or manifold on each end, which causes a sudden change in the cross-section following a 90°-bend (Fig. 3) from the pipe to the microchannel. This results in flow redirection and separation and generates a secondary flow along the microchannel, especially for high mass flow rates ($M > 20\ \mathrm{g\,min^{-1}}$). Fig. 11 shows the velocity profile in the entrance region of the microchannel, where both the streamwise (U_x) and the in-plane ($U_s = \sqrt{U_y^2 + U_z^2}$) velocities are normalized with the average velocity, which is computed based on the microchannel mass flux ($U_{ave} = G_{mc}/\rho$). At low mass flow rates, the velocity profile is rather uniform, while at higher mass flow rates, a stronger secondary flow emerges leading to flow asymmetry for the streamwise velocity component. The main streamwise velocity is, however, still much more influential than the secondary flow. The inlet condition of a microchannel has a significant impact on the length of the entrance region, especially at low mass flow rates. The flow undergoes a bending process as it enters the microchannel, and this bending contributes significantly to the developing zone in the entrance region. The size of the separated flow area varies depending on the mass flow rate, and it becomes more pronounced at higher flow rates. In Fig. 12, we present a comparison between the measured entrance lengths obtained from our numerical simulations and those reported in previous studies. To capture the relationship between mass flow rate and entrance length, we fitted a curve based on Eq. 8 using the selected mass flow rates, and the corresponding fitting parameters are provided in Tab. 3. Our findings reveal that the entrance region in our experimental setup is slightly longer than what has been reported in the existing literature. However, as the mass flow rate increases ($Re > 50$), the influence of the entrance condition on the length of the entrance region becomes insignificant compared to

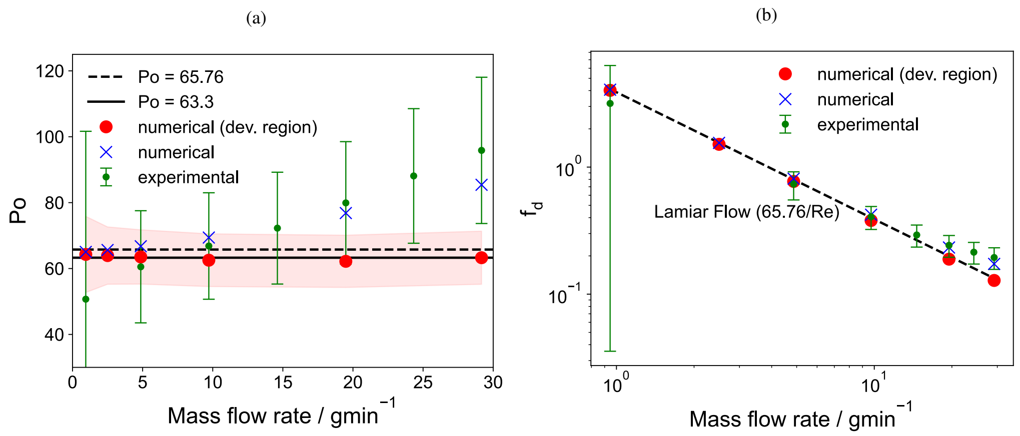

Figure 13: Comparison of (a) Poiseuille number and (b) friction factor from experimental data for the entire microchannel and numerical data computed for the entire microchannel and for the fully-developed region of the microchannel

the impact of the boundary layer. Consequently, for high mass flow rates, the estimated entrance length in our study aligns well with the values documented in the literature.

4.1.4. Friction factor and Poiseuille number

The Poiseuille number Po is defined as the product of the friction factor f and Reynolds number Re. It must be noted that in literature [15, 39], either the Fanning friction factor f_f or the Darcy friction factor f_d is employed as:

$$f_d = 4f_f = \frac{2\Delta P_{mc} D_h}{\rho L_{mc} U_{mc}^2}, \tag{10}$$

where $U_{mc} = M/\rho A_{mc}$ is the microchannel average inlet velocity. The Poiseuille number is constant for the laminar flow in a fully-developed region based on Stokes flow theory. Its value for circular tubes is $Po = f_d Re = 64$. For rectangular ducts, it can be also computed as [40]:

$$\begin{gathered} Po = f_d Re = 96\left(1.0 + \sum_{n=1}^{5} a_n AR^n\right), \\ a_1 = -1.3553, a_2 = 1.9467, a_3 = -1.7012, a_4 = 0.9564, a_5 = -0.2537, \end{gathered} \tag{11}$$

where for square ducts ($AR = 1$) Po is 56.9. In the present study, the nominal aspect ratio of the rectangular cross-section is 0.393, which gives $Po = 65.76$ (respectively $f_d = 65.76/Re$) according to Eq. 11. In Fig. 13a the Poiseuille number Po and in Fig. 13b the Darcy friction factor f_d is computed for both the numerical simulation and the experiment. They agree well with each other when the measurement uncertainty is taken into account. For both, Po increases and f_d decreases with increasing flow rate, thus appearing to deviate from Stokes flow macroscale theory.

The experimental deviation from $Po = f_d Re = const$ for various mass flow rates is a phenomenon that is also reported in previous studies [8, 41] for microchannels. It is often linked to

(a) RTD (b) T/C

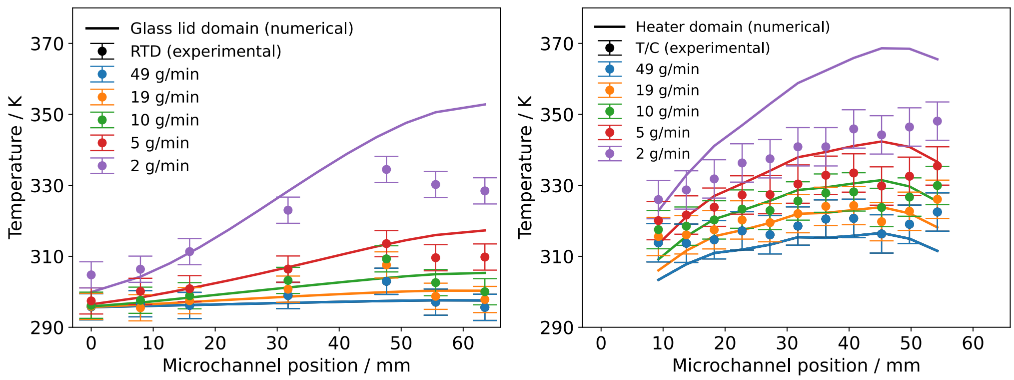

Figure 14: Measured and simulated temperature profiles along the microchannel from the inlet to the outlet: RTD and glass lid domain temperatures (a), T/C and heater domain temperatures (b). Wall temperature is plotted for numerical simulation.

viscous heating and fluid polarity [6]. In a study by Gian Luca Morini [18], it is reported, that viscous dissipation produces a non-negligible effect for liquid flows in microchannels with a hydraulic diameter smaller than 100 µm and leads to a decreasing Poiseuille number with increasing Reynolds number. However, in the isothermal experimental pressure measurements of this study in a microchannel with a hydraulic diameter of 848.9 µm, no viscous heating of the DI water is observed. The fluid temperature remains constant from the inlet to the outlet of the heat sink for all considered flow rates. Our numerical study, however, shows that in spite of the absence of viscous dissipation effects the Poiseuille can increase with increasing mass flow rate (Reynolds number), which is related to the length of the developing flow region. If the entrance length (L_e) is excluded from the total microchannel length L_{mc} and only the fully-developed region in the microchannel is considered, then Po remains constant at about 63.3. This is clearly visible in Fig. 13 from the numerical simulations that only consider the developed region. Hence, the consideration of flow development at the microchannel entrance might be crucial for an explanation of result deviations from the Stokes flow theory. The minor deviation from the theoretical value of $Po = 65.76$ calculated with Eq. 11 could be due either to the measurement uncertainty u_{Po} (see Eq. 39) mainly dominated by the uncertainty of the fit between heat sink and microchannel $u_{H_{fit}}$ (Tab. 1) or the shape of the microchannel cross-section, which is not perfectly rectangular due to the corner radii at the bottom edges. The uncertainty of the friction factor u_f as well as the uncertainty of the Poiseuille number u_{Po} (calculated with Eqs. 37-39) at the lowest flow rate of 1 g min^{-1} are estimated to be very high (Fig. 13). This is linked to the fact that they are in the first place dominated by the uncertainty of the pressure transducer $u_{p_{tot}}$ (Tab. 1). However, at a flow rate of 5 g min^{-1} or higher, the influence of $u_{\Delta p_{tot}}$ on the uncertainties u_f and u_{Po} becomes negligibly small so they are rather dominated by $u_{H_{fit}}$ and slightly increase with the squared mass flux G as explained in Section 4.1.2.

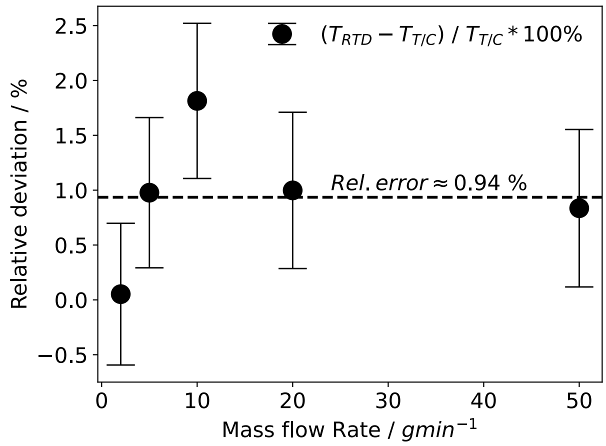

Figure 15: Relative deviation $(T_{RTD} - T_{T/C})/T_{T/C} \cdot 100$ % of the RTD temperature measurement at the outlet of the microchannel from the T/C type measurement of the liquid temperature 18 mm downstream at the heat sink outlet

4.2. Diabatic Study

4.2.1. Temperature Profile

Fig. 14a shows the temperature profile of the numerically simulated glass lid temperature profile together with the experimentally measured RTD temperatures from the inlet center (0 mm) to the outlet center (63.5 mm) of the microchannel. Fig. 14b shows the experimentally determined T/C temperatures at the tips of the cartridge heaters and the numerically simulated temperatures along the heater domain matching the positions of the T/C tips. The plotted standard deviation of the measured RTD and T/C temperatures is in the range of $3u$, so the measured values are expected to be within the plotted measurement uncertainty range with a probability of 99.7 %. It can be observed that for mass flow rates lower than 49 g min^{-1} the RTD and T/C temperatures mostly agree with the numerically simulated temperature along the glass lid and heater domain within an uncertainty of $3u$. However, in the range above 48 mm downstream of the microchannel inlet, the measured RTD temperature seems to drop, whereas the simulated glass lid temperature continues to increase with a slightly reduced slope. This is particularly evident when comparing the RTD measured temperature values with the simulated temperatures along the glass lid domain at 2 g min^{-1}. The experimentally measured T/C temperatures increase already from the beginning at the microchannel inlet with a significantly lower slope than the simulated heater domain temperatures for a flow rate of 2 g min^{-1}. It is hypothesized that the axial heat losses to the heat sink housing and the environment increase close to the microchannel outlet, which is underestimated in the numerical simulation due to the uncertainty of the introduced air heat transfer coefficient (more in Section 4.2.2). A similar heat loss is observed in a related heat sink design with a single stainless steel microchannel by Talebi *et al.* [42]. In the work of Talebi *et al.*, a significant drop in channel temperature of up to 10 °C occurs from the center to the outlet of the microchannel, which is linked to an increased heat loss at the outlet of the microchannel. To support this argument and to rule out a possible defect in the RTD structure at the microchannel outlet, in Fig. 15 the RTD measurement at the outlet of the microchannel was compared with the T/C type T fluid temperature measurement at the outlet of the heat sink housing 18 mm downstream of the microchannel outlet. The relative deviation between the two temperatures

(a) RTD (b) T/C

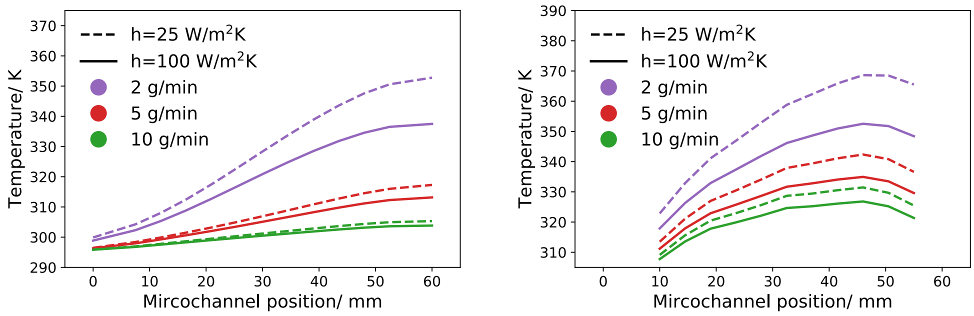

Figure 16: Impact of the chosen heat transfer coefficient h value on the simulated temperature profile

was on average only 0.9 %. It can therefore be assumed that the RTD temperature measured at the microchannel outlet approximates the fluid temperature at the heat sink outlet and correctly captures the data.

4.2.2. Air Heat Transfer Coefficient

In the present study, an air heat transfer coefficient (HTC) of $h = 25\ \mathrm{W\,m^{-2}\,K^{-1}}$ is initially assumed as suggested in [43] for the surrounding air in contact with the heat sink. However, it is important to note that the HTC for air is not fixed nor uniform and is primarily influenced by the surface temperature. In general, the HTC increases with a larger temperature difference between the air and the surface. This variability in HTC presents a significant source of uncertainty in heat transfer simulations.

As depicted in Fig 14a and Fig 14b, assuming a fixed HTC can lead to an underestimation of heat loss, especially in scenarios with low mass flow rates inside the heat sink where the surface temperature of the heat sink is higher. To further emphasize the impact of HTC variation, Fig 16b and Fig 16a illustrate the numerical temperature profile of the heater and glass lid domain for three different mass flow rates. The figure confirms that at lower mass flow rates the HTC has a significant impact on the result of the numerically simulated heater and glass lid domain temperatures. Conversely, at higher mass flow rates, where the surface temperature is lower, the uncertainty in the HTC has less influence on the overall result. Generally, the HTC uncertainty has a greater influence on the simulated heater domain temperature than on the glass lid domain temperature. Above a mass flow rate of 10 $\mathrm{g\,min^{-1}}$, the HTC of the simulated glass lid domain has a negligible influence on the temperature curve. This is confirmed by the surface temperature line profiles measured with the infrared camera along the external glass lid surface from the microchannel inlet to the microchannel outlet (Fig. 17c) and along the external heat sink surface from the first to the last heater cartridge (Fig. 17d). Fig. 17a and Fig. 17b show the corresponding infrared camera images of the heat sink top and heat sink front where the respective positions of the temperature line profiles are marked. A closer look at Fig. 17c and Fig. 17d confirms that at a low flow rate of 2 $\mathrm{g\,min^{-1}}$, the plotted external glass lid and heat sink surface temperatures are the highest and are therefore most likely to be affected by uncertainties of the estimated HTC. The measured surface temperatures of the glass lid and the heat sink front side drop considerably

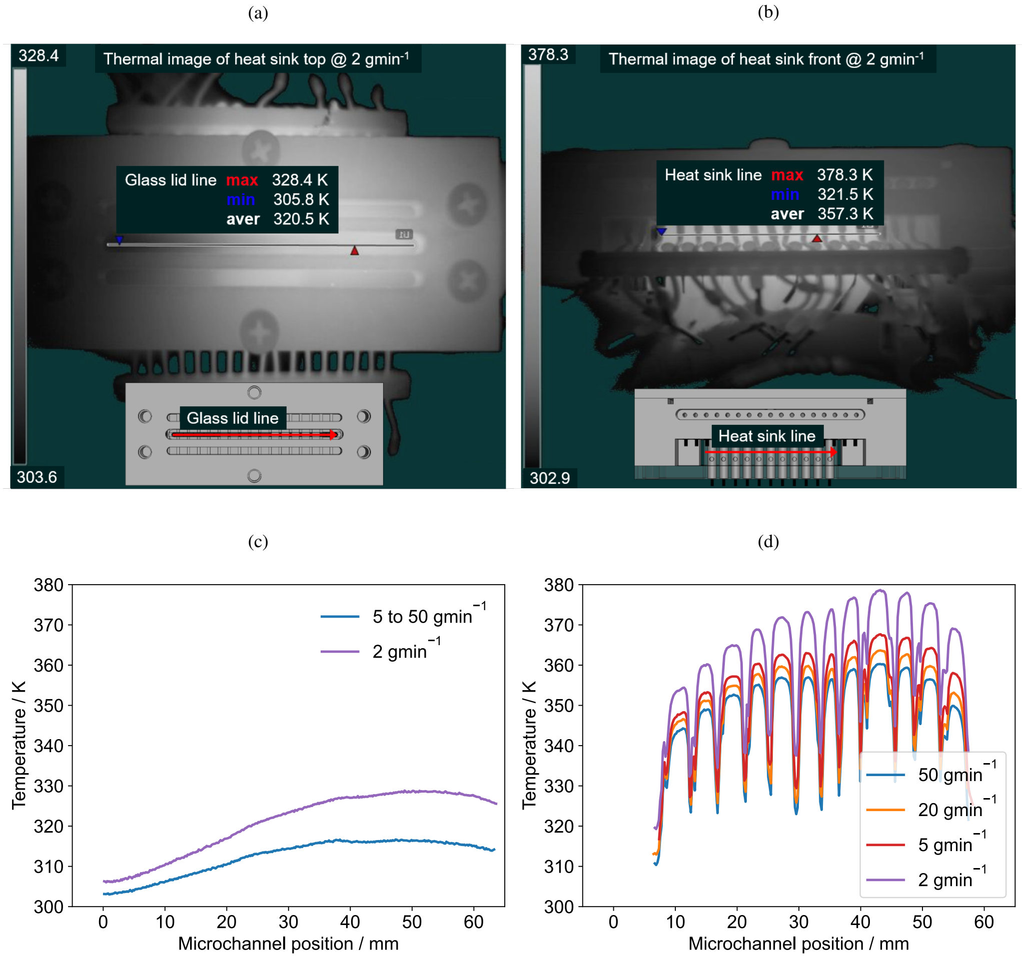

Figure 17: Thermal images at 2 g min^{-1} of the heat sink top with glass lid (a), of the heat sink front (b) with line markings of the respective temperature line profiles along the glass lid outside from the microchannel inlet to outlet (c) and along the heat sink front from the first cartridge heater to the last cartridge heater (d)

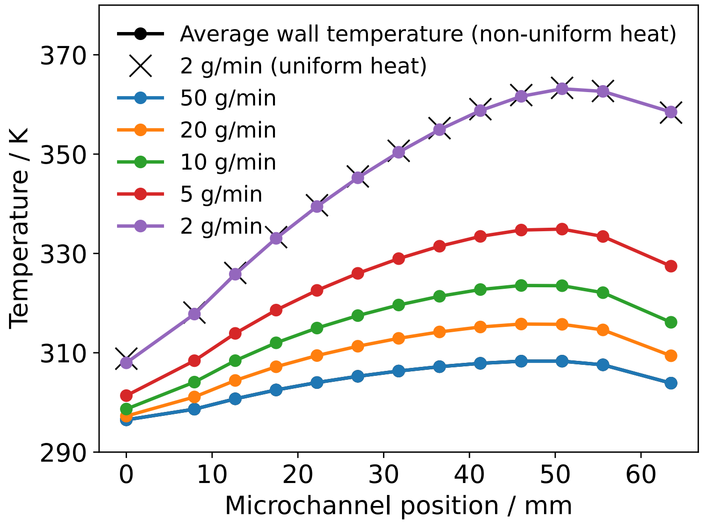

Figure 18: Numerical simulated average microchannel wall temperatures for non-uniform heat source assumption and at 2 g min^{-1} additionally for uniform heat source assumption

between 2 and 5 g min^{-1}. From 5 g min^{-1}, the surface temperature of the glass lid remains constant up to a mass flow rate of 50 g min^{-1}, whereas the surface temperature of the heat sink front continues to decrease, but at a rate that decreases with the mass flow rate. Based on a set of observations, it has to be concluded that proper estimation of HTC is crucial for obtaining accurate and reliable results in heat transfer simulations.

4.2.3. Non-Uniform Heat Source

To check the effect on variation in the provided heat source at particular cartridges, a non-uniform heat distribution is used based on the exactly measured heat output of each heater cartridge given in Section 2. Fig. 18 shows the numerically simulated average microchannel wall temperature from inlet to outlet with an additional uniform heat source temperature profile at 2 g min^{-1}. Due to the thermal conductivity of the SS microchannel (15 W m^{-1} K^{-1}), the difference in the temperature profile for a uniform and a non-uniform heat source was only marginal across all flow rates. This finding is interesting as it suggests that the standard deviation of ±4.4 % in heat power of the cartridge heaters does not significantly impact the temperature distribution in the microchannel and therefore is not leading to a disagreement between experiment and numerical simulation.

4.2.4. Heat Transfer Characteristics

The microchannel average wall temperatures for non-uniform heat in Fig. 18 were used for the calculation of the Nusselt numbers in this section. These temperatures are based on 3D heat transfer simulations using the experimentally determined heating power of each cartridge, and thus approximate the wall temperatures in this study more accurately than 1D or 2D heat transfer calculations. The thermal length can be estimated using:

$$\frac{L_{th}}{D_h} = c_{th} Re Pr, \tag{12}$$

(a) $h(x)$ (b) $Nu(x)$

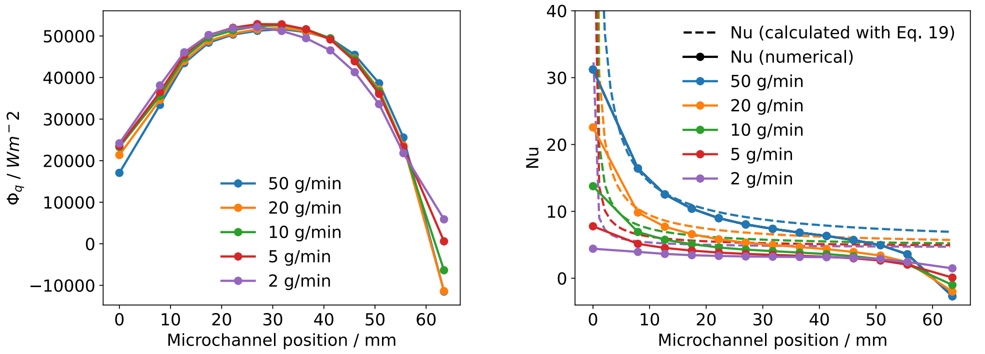

(c) h_{ave} (d) Nu_{av}

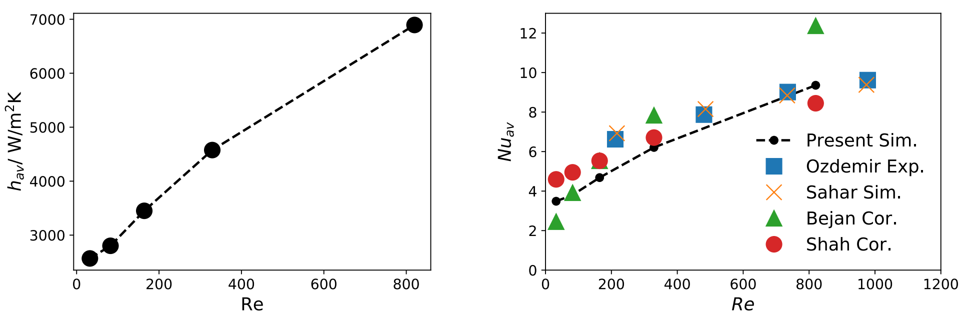

Figure 19: Simulated axial heat flux (a), simulated local Nusselt number compared with $Nu(x)$ (dashed lines) calculated with Equation 16 [44] (b), average heat transfer coefficient (c) and simulated average Nusselt number (d) for mass flow rates between 2 to 49 g/min

where c_{th} is the empirical coefficient and suggested to be chosen in the range from 0.028 to 0.116 for different microchannel aspect ratios [44]. Based on correlations from [44], for the present configuration at $AR = 0.393$, the coefficient is estimated to be $c_{th} = 0.0719$. This corresponds to thermal development length $L_{th} = 13.8, 35.1, 70.1, 140.6, 350.1$ mm for the mass flow rates of $M = 2, 5, 10, 20, 50$ g min^{-1}, respectively. However, due to the fact, that we never approach the thermally developed state in the considered system, we cannot confirm this estimations through numerical simulations or experiments.

The local Nusselt number Nu(x) in the numerical study is computed as:

$$Nu(x) = \frac{h(x) D_h}{\kappa_{av}}, \tag{13}$$

where κ_{av} is the fluid average thermal conductivity and the local heat transfer coefficient $h(x)$ is:

$$h(x) = \frac{\Phi_q(x)}{T_{w,av}(x) - T_{f,av}(x)}. \tag{14}$$

The wall heat flux $\Phi_q(x)$ along the axial direction and the local wall temperature $T_{w,av}(x)$ are computed by averaging all data values extracted using a line plotted along the width and height of the microchannel at the selected sections. The average fluid temperature $T_{f,av}(x)$ is defined as:

$$T_{f,av}(x) = \frac{\int_\Omega \rho c_p u T d\Omega}{\int_\Omega \rho c_p u d\Omega}, \tag{15}$$

where the sampling is done in the chosen cross-sections along the microchannel. The wall heat flux $\Phi_q(x)$ is plotted for various mass flow rates in Fig. 19a. The results confirm that the maximum heat transfer takes place in the middle of the microchannel, and the region near the outlet is not actively heated due to non-uniform heating conditions in our experimental setup, leading to a sharp heat flux drop at the end of the microchannel. The local $Nu(x)$ is plotted in Fig. 19b and compared with the following correlation [44]:

$$Nu(x) = Nu_{fd}\left(1.0 + \left(\frac{0.0134}{x^{*0.631}}\right)\right), \tag{16}$$

where

$$x^* = \left(\frac{x}{D_h} \frac{AR^{0.583}}{RePr}\right)^{1.2}, \tag{17}$$

and the fully developed Nusselt number $Nu_{fd} = 4.5$ for constant heat flux in a rectangular channel at $AR = 0.39$ is assumed [45]. The observed deviation from the correlation at the outlet of the microchannel is attributed to the nonuniform heat flux conditions in our setup.

The average heat transfer coefficient and the average Nusselt number are defined as:

$$h_{av} = \frac{1}{L_{mc}} \int_0^{L_{mc}} h(x) dx, \tag{18}$$

$$Nu_{av} = \frac{h_{av} D_h}{k_{av}}. \tag{19}$$

As depicted in Fig. 19c, we observe that h_{av} increases with the mass flow rate (Re), indicating that flow is thermally developing. To further verify this trend, we compare our simulated results of the average Nusselt number Nu_{av}, as shown in Fig. 19d, with experimental data obtained by Ozdemir *et al.* [46] and numerical results reported by Sahar *et al.* [15]. Both of these studies investigated laminar flow in microchannels with a similar aspect ratio to that of our present study. Furthermore, we compare our simulation results with the correlations proposed by Bejan [47] (Eq. 20) and Shah and London [40] (Eq. 21), which predict the Nusselt number for thermally developing laminar flow. This comparison allows us to confirm that our simulations are consistent with previous studies.

$$Nu_{av} = 1.375 Pe^{*,1/2}, \tag{20}$$

$$Nu_{av} = \begin{cases} 4.364 + 0.0722 Pe^{*} & Pe^{*} < 33, \\ 1.953 Pe^{*1/3} & Pe^{*} \geqslant 33. \end{cases} \tag{21}$$

where $Pe^{*} = RePrD_h/L_{mc}$. The deviation observed between the presented data and previous studies can be attributed to differences in experimental/numerical setup. In our present investigation, it is noteworthy that the heat flux distribution is non-uniform, which deviates from the assumptions of perfect uniform heat flux made in prior numerical studies. Furthermore, our system exhibits a non-rectangular cross section (small rounded corners at the bottom of microchannel wall), in contrast to idealized geometries assumed in previous research. Additionally, we take into account the minor heat losses through the glass lid, a factor that was rarely considered or considered as adiabatic boundary condition in previous studies.

5. SUMMARY

The pressure drop, temperature profile and heat transfer of a heat sink with a single stainless steel microchannel with a hydraulic diameter of 848.9 μm has been studied experimentally and numerically for DI water flow at various flow rates. The inconsistencies between experiments and numerical results have been examined in order to understand their roots and develop a set of rules for a successful handshake between simulation and experiment.

The numerically simulated pressure drop is found to be well within the range of experimental measurement uncertainties after the nominal geometry has been adjusted to take into account the realistic details of the setup – the corner radius of 0.2 mm at the edges of the microchannel bottom and the 100 μm larger height representing the unavoidable gap between the glass lid and the metal block. Furthermore, the total measured pressure loss has been corrected taking into account the additional pressure losses at the inlet and outlet manifold using correlation-based loss factors. A closer look at the laminar flow development from the inlet to the outlet of the microchannel demonstrates that already from a flow rate of 20 $\mathrm{g\,min^{-1}}$ half of the channel length is needed until the laminar flow reaches a fully developed state. The development of the flow is mainly governed by the presence of the channel bend at the inlet of the microchannel system, which induces 3-dimensional pattern in the flow field and promotes a formation of a growing boundary layer downstream of the bend. The presence of developing region leads to an increasing Poiseuille number at higher mass flow rates and hence introduces a disagreement compared to the laminar flow theory, where Po is supposed to remain constant. Considering only the fully developed microchannel region, the Poiseuille number is demonstrated to be constant at 65.8 and shows no deviation from the laminar flow theory. Overall, it can be concluded, that the experimental measurement uncertainties of the pressure drop and the Poiseuille number are largely determined by the appropriate prescription of the microchannel cross section and its geometrical details.

The agreement between simulated and measured temperature profiles at the heater and glass lid improves as the flow rate increases. The largest deviation between numerically simulated and experimentally measured temperatures is found in the area of the microchannel outlet. Presumably, this is linked to the estimation of the prescribed heat transfer coefficient of the ambient air in the simulation, as the coefficient increases with increasing temperature gradients. Since the heat sink surface temperature is highest at low flow rates and increases from the microchannel inlet to the outlet, the largest temperature gradient occurs at the lowest flow rate of 2 $\mathrm{g\,min^{-1}}$ in the area of the microchannel outlet. The chosen heat transfer coefficient of 25 $\mathrm{W\,m^{-2}\,K^{-1}}$ thus underestimates the heat transfer between ambient air and heat sink of the experiment at low flow rates in the outlet area of the microchannel, while it reliably estimates the heat transfer in the remaining area of the microchannel at higher flow rates.

The determined local Nusselt number compares well to the correlations for the laminar flow of DI water, except for the values near the channel outlet, which is again related to the choice of heat transfer coefficient at the boundaries of the simulation domain. This underscores the importance of prescribing accurate non-homogeneous thermal boundary conditions in numerical simulations as a crucial factor for faithfully capturing all the experimental aspects of the process.

Concluding, we identify the geometrical description of the microchannel geometry including plenum design of the inlet/outlet of the system together with the knowledge about the flow state (developing or developed) as the most significant factors for the experimental-numerical handshake in terms of pressure drop estimation. Additionally, the proper choice of the thermal boundary condition at the outer boundary remains the most important factor for a proper prediction of the heat transfer behavior in microchannel systems.

FUNDING

This work was funded by the German Research Foundation (DFG) through the Research Unit 2383 ProMiSe under Grant No. STR 1585/2-1 and WO 883/24-2.

REFERENCES

[1] Zhang, L., Goodson, K., and Kenny, T., 2004, *Silicon microchannel heat sinks: theories and phenomena* Springer Science & Business Media.

[2] Ramesh, K. N., Sharma, T. K., and Rao, G. A. P., 2021, "Latest advancements in heat transfer enhancement in the micro-channel heat sinks: a review," *Archives of Computational Methods in Engineering,* **28**, pp. 3135–3165.

[3] Coskun, T., and Cetkin, E., 2020, "A review of heat and fluid flow characteristics in microchannel heat sinks," *Heat Transfer,* **49**(8), pp. 4109–4133.

[4] Peng, X., and Peterson, G., 1995, "The effect of thermofluid and geometrical parameters on convection of liquids through rectangular microchannels," *International Journal of Heat and Mass Transfer,* **38**(4), pp. 755–758.

[5] Xu, B., Ooti, K., Wong, N., and Choi, W., 2000, "Experimental investigation of flow friction for liquid flow in microchannels," *International Communications in Heat and Mass Transfer,* **27**(8), pp. 1165–1176.

[6] Judy, J., Maynes, D., and Webb, B., 2002, "Characterization of frictional pressure drop for liquid flows through microchannels," *International Journal of heat and mass transfer,* **45**(17), pp. 3477–3489.

[7] Rosa, P., Karayiannis, T., and Collins, M., 2009, "Single-phase heat transfer in microchannels: The importance of scaling effects," *Applied Thermal Engineering,* **29**(17-18), pp. 3447–3468.

[8] Peng, X., Peterson, G., and Wang, B., 1994, "Frictional flow characteristics of water flowing through rectangular microchannels," *Experimental Heat Transfer An International Journal,* **7**(4), pp. 249–264.

[9] Pfund, D., Rector, D., Shekarriz, A., Popescu, A., and Welty, J., 2000, "Pressure drop measurements in a microchannel," *AIChE Journal,* **46**(8), pp. 1496–1507.

[10] Mokrani, O., Bourouga, B., Castelain, C., and Peerhossaini, H., 2009, "Fluid flow and convective heat transfer in flat microchannels," *International Journal of Heat and Mass Transfer,* **52**(5-6), pp. 1337–1352.

[11] Lee, P.-S., Garimella, S. V., and Liu, D., 2005, "Investigation of heat transfer in rectangular microchannels," *International journal of heat and mass transfer,* **48**(9), pp. 1688–1704.
[12] Sahar, A. M., Özdemir, M. R., Fayyadh, E. M., Wissink, J., Mahmoud, M. M., and Karayiannis, T. G., 2016, "Single phase flow pressure drop and heat transfer in rectangular metallic microchannels," *Applied Thermal Engineering,* **93**, pp. 1324–1336.
[13] Dharaiya, V., and Kandlikar, S. G., 2012, "Numerical investigation of heat transfer in rectangular microchannels under h2 boundary condition during developing and fully developed laminar flow," *Journal of heat transfer,* **134**(2).
[14] Gunnasegaran, P., Mohammed, H., Shuaib, N., and Saidur, R., 2010, "The effect of geometrical parameters on heat transfer characteristics of microchannels heat sink with different shapes," *International communications in heat and mass transfer,* **37**(8), pp. 1078–1086.
[15] Sahar, A. M., Wissink, J., Mahmoud, M. M., Karayiannis, T. G., and Ishak, M. S. A., 2017, "Effect of hydraulic diameter and aspect ratio on single phase flow and heat transfer in a rectangular microchannel," *Applied Thermal Engineering,* **115**, pp. 793–814.
[16] Pan, Y.-H., Zhao, R., Fan, X.-H., Nian, Y.-L., and Cheng, W.-L., 2020, "Study on the effect of varying channel aspect ratio on heat transfer performance of manifold microchannel heat sink," *International Journal of Heat and Mass Transfer,* **163**, p. 120461.
[17] Hetsroni, G., Mosyak, A., Pogrebnyak, E., and Yarin, L., 2005, "Fluid flow in micro-channels," *International Journal of Heat and Mass Transfer,* **48**(10), pp. 1982–1998.
[18] Morini, G. L., 2005, "Viscous heating in liquid flows in micro-channels," *International journal of heat and mass transfer,* **48**(17), pp. 3637–3647.
[19] Co., W. E. M., 2016, 1/8-inch firerod® cartridge heaters Accessed: 29 Sept. 2022.
[20] Schepperle, M., Ghanam, M., Bucherer, A., Gerach, T., and Woias, P., 2022, "Noninvasive platinum thin-film microheater/temperature sensor array for predicting and controlling flow boiling in microchannels," *Sensors and Actuators A: Physical,* **345**, p. 113811.
[21] Schepperle, M., Samkhaniani, N., Magnini, M., Woias, P., and Stroh, A., 2022, "Thermohydraulic characterization of di water flow in rectangular microchannels by means of experiments and simulations," In Proceedings of the 7 Th World Congress on Momentum, Heat and Mass Transfer (MHMT'22), Virtual.
[22] Schepperle, M., Junaid, S., Mandal, A., Selvam, D., and Woias, P., 2022, "Determination of void fraction in microchannel flow boiling using computer vision," In Proceedings of the 8 Th World Congress on Mechanical, Chemical, and Material Engineering (MCM'22).
[23] Schepperle, M., Mandal, A., and Woias, P., 2023, "Flow boiling instabilities and single-phase pressure drop in rectangular microchannels with different inlet restrictions," In Proceedings of the 8 Th World Congress on Momentum, Heat and Mass Transfer (MHMT'23).
[24] Mikrosysteme, H. Productinformation mzr-4622 Accessed: 29 Sept. 2022.
[25] Formlabs, 2020, Rigid 10k resin for rigid, strong, industrial-grade prototypes Accessed: 29 Sept. 2022.
[26] uwe electronic GmbH, 2021, Battery probe - uebk-12613 Accessed: 29 Sept. 2022.
[27] AG, K. D., 2017, Differential pressure transmitters series prd-33 x Accessed: 29 Sept. 2022.
[28] Lee, P.-S., and Garimella, S. V., 2008, "Saturated flow boiling heat transfer and pressure drop in silicon microchannel arrays," *International Journal of Heat and Mass Transfer,* **51**(3-4), pp. 789–806.
[29] Incropera, F. P., DeWitt, D. P., Bergman, T. L., Lavine, A. S., et al., 1996, *Fundamentals of heat and mass transfer*, Vol. 6 Wiley New York.
[30] Deutsches Institut für Normung e.V., 1996, *Fundamentals of metrology - Part 3: Evaluation of measurements of a single measurand, measurement uncertainty* Beuth Verlag GmbH.
[31] Weller, H. G., Tabor, G., Jasak, H., and Fureby, C., 1998, "A tensorial approach to computational continuum mechanics using object-oriented techniques," *Computers in physics,* **12**(6), pp. 620–631.
[32] Atkinson, B., Brocklebank, M., Card, C., and Smith, J., 1969, "Low reynolds number developing flows," *AIChE Journal,* **15**(4), pp. 548–553.
[33] Galvis, E., Yarusevych, S., and Culham, J., 2012, "Incompressible laminar developing flow in microchannels," *Journal of fluids engineering,* **134**(1).
[34] Ahmad, T., and Hassan, I., 2010, "Experimental analysis of microchannel entrance length characteristics using microparticle image velocimetry," *Journal of fluids engineering,* **132**(4).
[35] Chen, R.-Y., 1973, "Flow in the entrance region at low reynolds numbers,".
[36] Li, H., Huang, B., and Wu, M., 2019, "Experimental and numerical investigations on the flow characteristics within hydrodynamic entrance regions in microchannels," *Micromachines,* **10**(5), p. 317.
[37] Lobo, O. J., and Chatterjee, D., 2022, "Effect of aspect ratio on entrance length in rectangular minichannels with plenum," *Physics of Fluids,* **34**(11), p. 112009.
[38] Joshi, Y., and Vinoth, B., 2018, "Entry lengths of laminar pipe and channel flows," *Journal of Fluids Engineering,* **140**(6).
[39] Delplace, F., 2018, "Laminar flow of newtonian liquids in ducts of rectangular cross-section a model for both

physics and mathematics," *Open Access J. Math. Theor. Phys.,* **1**(5), pp. 198–201.
[40] Shah, R. K., and London, A. L., 2014, *Laminar flow forced convection in ducts: a sourcebook for compact heat exchanger analytical data* Academic press.
[41] Peng, X., and Peterson, G., 1996, "Convective heat transfer and flow friction for water flow in microchannel structures," *International journal of heat and mass transfer,* **39**(12), pp. 2599–2608.
[42] Talebi, M., Sadir, S., Kraut, M., Dittmeyer, R., and Woias, P., 2020, "Local heat transfer analysis in a single microchannel with boiling di-water and correlations with impedance local sensors," *Energies,* **13**(23), p. 6473.
[43] Kosky, P., Balmer, R., Keat, W., and Wise, G., 2013, "Chapter 12 - mechanical engineering," In *Exploring Engineering (Third Edition)*, P. Kosky, R. Balmer, W. Keat, and G. Wise, eds., third edition ed. Academic Press, Boston, pp. 259–281.
[44] El-Genk, M. S., and Pourghasemi, M., 2019, "Nusselt number and development length correlations for laminar flows of water and air in microchannels," *International Journal of Heat and Mass Transfer,* **133**, pp. 277–294.
[45] Lee, P.-S., and Garimella, S. V., 2006, "Thermally developing flow and heat transfer in rectangular microchannels of different aspect ratios," *International journal of heat and mass transfer,* **49**(17-18), pp. 3060–3067.
[46] Ozdemir, M., and Mahmoud, M., 2016, "Flow boiling heat transfer in a rectangular copper microchannel,".
[47] Bejan, A., 2013, *Convection heat transfer* John wiley & sons.
[48] Kell, G. S., 1975, "Density, thermal expansivity, and compressibility of liquid water from 0. deg. to 150. deg.. correlations and tables for atmospheric pressure and saturation reviewed and expressed on 1968 temperature scale," *Journal of Chemical and Engineering data,* **20**(1), pp. 97–105.
[49] Jones, F. E., and Harris, G. L., 1992, "Its-90 density of water formulation for volumetric standards calibration," *Journal of research of the National Institute of Standards and Technology,* **97**(3), p. 335.
[50] Viswanath, D., and Natarajan, G., 1989, "Data book on the viscosity of liquids, hemisphere pub," *Corp., New York, NY*, p. 990.
[51] Popiel, C., and Wojtkowiak, J., 1998, "Simple formulas for thermophysical properties of liquid water for heat transfer calculations (from 0 c to 150 c)," *Heat transfer engineering,* **19**(3), pp. 87–101.

APPENDIX A. ESTIMATION OF PRESSURE LOSSES AND MATERIAL PROPERTIES

The pressure loss due to flow contraction Δp_{in} at the microchannel inlet 90° bend (with $A_{mc} < A_{in}$) and flow expansion Δp_{out} at the microchannel outlet 90° bend (with $A_{out} > A_{mc}$) as depicted in Fig. 3, are calculated using the data reduction method by Lee and Garimella (2008) [28]:

- pressure loss due to contraction at microchannel inlet

$$\Delta p_{in} = \left[1 - \left(\frac{A_{mc}}{A_{in}}\right)^2 + K_{cont}\right] \frac{G_{mc}^2}{2\rho}, \tag{21}$$

  with the loss coefficient

$$K_{cont} = 0.0088\,(AR)^2 - 0.1785\,(AR) + 1.6027. \tag{22}$$

- pressure recovery due to expansion at microchannel outlet

$$\Delta p_{out} = \frac{1}{2} K_{exp} \frac{G^2}{2\rho}, \tag{23}$$

  with the loss coefficient

$$K_{exp} = -2 \cdot 1.33 \left(\frac{A_{mc}}{A_{out}}\right)\left[1 - \left(\frac{A_{mc}}{A_{out}}\right)\right]. \tag{24}$$

The following dimensions and properties are considered for evaluation:

- height of the microchannel $H = H_{mc} + H_{fit}$ including the gap to the glass lid: 592 ± 50 µm;
- microchannel width W_{mc}: 1500 ± 1 µm;
- aspect ratio $AR = H/W_{mc}$: 0.395 ± 0.033;
- cross-sectional area of the microchannel $A_{mc} = (H_{mc} + H_{fit})W_{mc}$: 0.888 ± 0.075 mm^2;
- area of the microchannel inlet and outlet $A_{in} = A_{out} = \pi(d_{in}/2)^2 = \pi(d_{out}/2)^2$: 1.767 mm^2;
- mass flux $G_{mc} = M/[(H_{mc}+H_{fit})W_{mc}]$ of the DI water inside the microchannel in kg m^{-2} s^{-1};
- density of water at 22.7 ± 1.1 °C ρ: 997.6 ± 0.3 kg m^{-3}.

The density of water was calculated with a simplified version of the formulation of Kell (1975) [48]. This formula was first published in [49] and is valid for air-free water at a pressure of 101.325 kPa (1 atmosphere) and 5 to 40 °C:

$$\rho(T) = a_1 + a_2 T \cdot 10^{-2} - a_3 T^2 \cdot 10^{-3} + a_4 T^3 \cdot 10^{-5} - a_5 T^4 \cdot 10^{-7}. \tag{25}$$

with $a_1 = 999.8531$, $a_2 = 6.3269$, $a_3 = 8.5238$, $a_4 = 6.9432$, $a_5 = 3.8212$.

The dynamic viscosity of water was calculated using the Vogel–Fulcher-Tammann equation given below [50]:

$$\mu(T) = A \cdot 10^{-3} \cdot \exp \frac{B}{T - C}, \tag{26}$$

with the corresponding coefficients for water $A = 0.02939$ Pa s, $B = 507.88$ K, $C = 149.3$ K.

The specific heat of water at constant pressure was calculated with an approximated measurement uncertainty of ±0.04 % with the following formula defined in [51] and given below:

$$c_p(T) = a + bT + cT^{1.5} + dT^2 + eT^{2.5}, \tag{27}$$

with $a = 4.2174356$, $b = -0.0056181625$, $c = 0.0012992528$,
$d = -0.00011535353$ and $e = 4.14964 \cdot 10^{-6}$.

APPENDIX B. MEASUREMENT UNCERTAINTIES

The following estimation for measurement uncertainties is utilized for the metrological characterization:

- microchannel cross-sectional area

$$u_{A_{mc}} = A_{mc} \cdot \sqrt{\left(\frac{u_H}{H}\right)^2 + \left(\frac{u_W}{W}\right)^2} \tag{28}$$

- microchannel hydraulic diameter

$$u_{D_h} = \frac{2 \cdot A_{mc}}{H + W} \cdot \sqrt{\left(\frac{u_{A_{mc}}}{A_{mc}}\right)^2 + \frac{u_H^2 + u_W^2}{(H + W)^2}} \tag{29}$$

- microchannel inlet/outlet area

$$u_{A_{in}} = \frac{\pi}{2} \cdot d_{in}^2 \cdot u_{d_{in}} \quad \text{or} \quad u_{A_{out}} = \frac{\pi}{2} \cdot d_{out}^2 \cdot u_{d_{out}} \tag{30}$$

- microchannel mass flux

$$u_G = G \times \sqrt{\left(\frac{u_M}{M}\right)^2 + \left(\frac{u_{H_{mc}}}{H_{mc}}\right)^2 + \left(\frac{u_{W_{mc}}}{W_{mc}}\right)^2} \tag{31}$$

- density of water

$$u_\rho = \Big|\Big(a_2 \cdot 10^{-2} - 2a_3 T \cdot 10^{-3} \ldots \\ +3a_4 T^2 \cdot 10^{-5} - 4a_5 T^3 \cdot 10^{-7}\Big) \cdot u_T\Big| \tag{32}$$

- dynamic viscosity of water

$$u_\mu = \sqrt{\left(\frac{-A \cdot B \cdot e^{B/(T-C)}}{1000 \cdot (T-C)^2} \cdot u_T\right)^2} \tag{33}$$

- pressure loss due to contraction at inlet

$$u_{\Delta p_{in}} = \left(\left(\frac{A_{mc}}{A_{in}}\right)^2 + K_{cont}\right) \cdot \frac{G^2}{2\rho} \ldots \\ \cdot \left[\frac{4 \cdot \left(\frac{A_{mc}}{A_{in}}\right)^2 \cdot \left(\left(\frac{u_{A_{mc}}}{A_{mc}}\right)^2 + \left(\frac{u_{A_{in}}}{A_{in}}\right)^2\right) \ldots + \left(0.0176\left(\frac{H}{W}\right)^2 - 0.1785\left(\frac{H}{W}\right)\right)^2 \cdot \left(\left(\frac{u_H}{H}\right)^2 + \left(\frac{u_W}{W}\right)^2\right)}{\left(\left(\frac{A_{mc}}{A_{in}}\right)^2 + K_{cont}\right)^2} \ldots \right. \\ \left. +4 \cdot \left(\left(\frac{u_M}{M}\right)^2 + \left(\frac{u_H}{H}\right)^2 + \left(\frac{u_W}{W}\right)^2\right) + \left(\frac{u_\rho}{\rho(T)}\right)^2\right]^{1/2} \tag{34}$$

- pressure recovery due to expansion at outlet

$$u_{\Delta p_{out}} = \frac{1}{2} \cdot K_{exp} \cdot \frac{G^2}{2\rho} \cdot \left[\frac{\left(-2.66 + 5.32\left(\frac{A_{mc}}{A_{out}}\right)\right)^2 \dots \cdot \left(\frac{A_{mc}}{A_{out}}\right)^2 \cdot \left(\left(\frac{u_{A_{mc}}}{A_{mc}}\right)^2 + \left(\frac{u_{A_{out}}}{A_{out}}\right)^2\right)}{K_{exp}^2} \dots \right.$$

$$\left. +4 \cdot \left(\left(\frac{u_M}{M}\right)^2 + \left(\frac{u_H}{H}\right)^2 + \left(\frac{u_W}{W}\right)^2\right) + \left(\frac{u_\rho}{\rho(T)}\right)^2 \right]^{1/2} \quad (35)$$

- pressure drop of microchannel

$$u_{\Delta p_{mc}} = \sqrt{u_{\Delta p_{tot}}^2 + u_{\Delta p_{in}}^2 + u_{\Delta p_{out}}^2} \quad (36)$$

- friction factor of microchannel

$$u_f = 2 \cdot \Delta p \cdot \frac{D_h}{L} \cdot \rho \cdot \left(\frac{A_{mc}}{M}\right)^2 \cdot \left[\left(\frac{u_{\Delta p_{mc}}}{\Delta p}\right)^2 + \left(\frac{u_{D_h}}{D_h}\right)^2 \dots \right.$$

$$\left. + \left(\frac{u_L}{L}\right)^2 + \left(\frac{u_\rho}{\rho}\right)^2 + 4 \cdot \left(\left(\frac{u_{A_{mc}}}{A_{mc}}\right)^2 + \left(\frac{u_M}{M}\right)^2\right)\right]^{0.5} \quad (37)$$

- Reynolds number of microchannel

$$u_{Re} = Re \cdot \sqrt{\left(\frac{u_M}{M}\right)^2 + \left(\frac{u_{A_{mc}}}{A_{mc}}\right)^2 + \left(\frac{u_{D_h}}{D_h}\right)^2 + \left(\frac{u_\mu}{\mu}\right)^2} \quad (38)$$

- Poiseuille number of microchannel

$$u_{Po} = Po \cdot \sqrt{\left(\frac{u_f}{f}\right)^2 + \left(\frac{u_{Re}}{Re}\right)^2} \quad (39)$$

APPENDIX C. INFLUENCE OF NUMERICAL SCHEME ORDER

It is widely recognized that first-order numerical schemes provide stability, albeit at the cost of increased numerical diffusion. In order to obtain higher accuracy, second-order schemes such as linearUpwind for the momentum equation and limitedLinear for the energy equation have been employed for two distinct flow regimes: low-speed flow at 2 g/Min and high-speed flow at 49 g/Min. Despite this, the application of second-order schemes did not yield a significant improvement in the temperature profiles at the locations of the T/Cs and RTDs as depicted in Fig. 20.

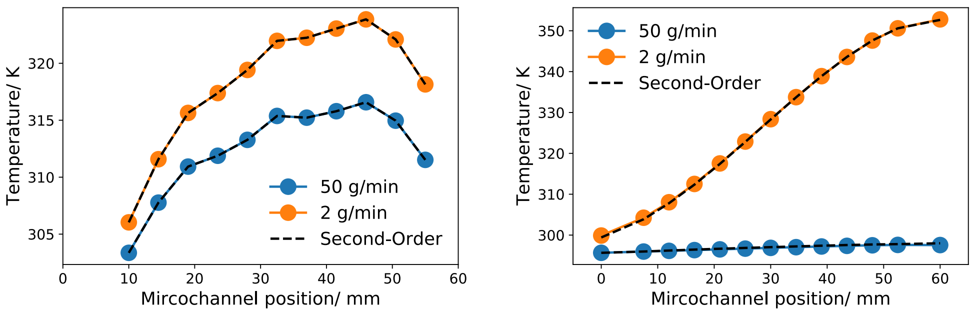

(a) T/C

(b) RTD

Figure 20: The temperature profile with first-order schemes. The result for second-order simulations is plotted with a black dashed line.